Icarus 318 (2019) 75–98

Contents lists available at ScienceDirect

Icarus

journal homepage: www.elsevier.com/locate/icarus

Spectral analysis of the Cerean geological unit *crater central peak material* as an indicator of subsurface mineral composition

A. Galiano[a,b,*], E. Palomba[a,c], A. Longobardo[a,d], M.C. De Sanctis[a], F.G. Carrozzo[a], A. Raponi[a], F. Tosi[a], E. Ammannito[e], E.A. Cloutis[f], C.A. Raymond[g], C.T. Russell[h], the VIR team

[a] *IAPS-INAF, Via del Fosso del Cavaliere, 100, 00133 Rome, Italy*
[b] *Università degli Studi di Roma Tor Vergata, Via della Ricerca Scientifica, 1, 00133 Rome, Italy*
[c] *ASI-SSDC, Via del Politecnico snc, 00133 Rome, Italy*
[d] *Università Parthenope, Via Ammiraglio Ferdinando Acton, 38, 80133 Naples, Italy*
[e] *ASI-URS, Via del Politecnico snc, 00133 Rome, Italy*
[f] *Department of Geography, University of Winnipeg, 515 Portage Ave, Winnipeg, Manitoba R3B 2E9, Canada*
[g] *JPL, California Institute of Technology, 4800 Oak Grove Dr, Pasadena, CA 91109, USA*
[h] *UCLA, Los Angeles, CA 90095, USA*

ARTICLE INFO

Keywords:
Asteroid Ceres
Mineralogy
Spectroscopy
Ceres interiors

ABSTRACT

The dwarf planet Ceres is a heavily cratered rocky body, and complex craters with a central peak are widely observed on its surface. These types of craters form when a large body impacts the surface, generating extreme temperatures and pressures. During the impact event a large volume of rock is raised from the subsurface and a central uplift is formed. The material composing the central uplift is called crater central peak material (ccp) and the spectral analysis of such geologic areas can provide information about the composition of Ceres' subsurface. Reflectance spectra of 32 ccps, acquired by the VIR spectrometer on board the NASA/Dawn spacecraft, were analyzed and shows absorption bands located at about 2.7, 3.1, 3.4 and 4.0 μm which are also common on the Cerean surface. These absorptions are related, respectively, to Mg-phyllosilicates, NH_4-phyllosilicates and Mg/Ca-carbonates.

The spectral parameters considered in this work are: spectral slopes estimated between 1.2 μm and 1.9 μm, band depths at 2.7-, 3.1-, 3.4- and 4.0-μm, and band centers near 4.0-μm. The ccps spectral parameters were analyzed in conjunction with other Cerean parameters, such as the estimated depth of excavation of the material composing the central peak, in order to search for correlations and information about Ceres' subsurface.

Central peak material located polewards show stronger 2.7- and 3.1-μm band depths with respect to those at the equatorial region, suggesting that subsurface deposits closer to poles are probably richer in Mg- and NH_4-phyllosilicates. The 3.4-μm spectral feature is also deeper in ccps located at poleward latitudes, similar to the phyllosilicates. Conversely, the 4.0-μm band does not show this trend with latitude.

An increase in both 3.1- and 3.4-μm band depths with the estimated depth of excavation indicates that the spectral feature at 3.4-μm is the result of different contributions from carbonates and NH_4-phyllosilicates, as expected. However, depending on their relative influence, the shape of the 3.4-μm spectral feature can vary.

Phyllosilicates and carbonates are the resulting products of aqueous alteration of chondritic material and, given the increasing abundance of such minerals (in particular ammoniated phyllosilicates) with depth of excavation, it is likely that our investigation involved subsurface layers nearby the boundary between the volatile-rich crust and the silicate-rich mantle.

Na-carbonate is found in the crater central peak material of Ernutet, Haulani and Ikapati, characterized by an estimated depth of excavation of about 6–9 km, where deposits of sodium carbonates could be locally present.

* Corresponding author at: IAPS-INAF, Via del Fosso del Cavaliere, 100, 00133 Rome, Italy.
E-mail addresses: anna.galiano@iaps.inaf.it (A. Galiano), ernesto.palomba@iaps.inaf.it (E. Palomba), andrea.longobardo@iaps.inaf.it (A. Longobardo), mariacristina.desanctis@iaps.inaf.it (M.C. De Sanctis), giacomo.carrozzo@iaps.inaf.it (F.G. Carrozzo), andrea.raponi@iaps.inaf.it (A. Raponi), federico.tosi@iaps.inaf.it (F. Tosi), eleonora.ammannito@asi.it (E. Ammannito), e.cloutis@uwinnipeg.ca (E.A. Cloutis), carol.a.raymond@jpl.nasa.gov (C.A. Raymond), ctrussell@igpp.ucla.edu (C.T. Russell).

https://doi.org/10.1016/j.icarus.2018.05.020
Received 27 February 2018; Received in revised form 7 May 2018; Accepted 23 May 2018
Available online 15 June 2018

1. Introduction

The dwarf planet Ceres has been widely investigated since March 2015, when NASA's Dawn spacecraft (Russell et al., 2016) arrived at Ceres and acquired images, hyperspectral data and elemental distributions by using the Framing Camera (FC), the Visible and Infrared Mapping Spectrometer (VIR) and the Gamma Ray and Neutron Detector (GRaND), respectively.

Through analysis of VIR data (De Sanctis et al., 2015; Ammannito et al., 2016), absorption bands at ~2.7, ~3.1, ~3.4 and ~4.0 μm have been identified in Cerean reflectance spectra. Simulations of Cerean spectra (by applying a Hapke based model) suggest that the surface is composed of Mg-phyllosilicates (such as antigorite), ammoniated phyllosilicates (such as NH_4-annite or NH_4-montmorillonite), Ca/Mg-carbonates (such as dolomite, magnesite or calcite) and a dark featureless material (De Sanctis et al., 2015). The ~2.7 μm feature is due to the hydroxide of Mg-phyllosilicates (De Sanctis et al., 2015), and the ~3.1 μm band is attributed to NH_4-bearing clays (De Sanctis et al., 2016). The ~3.4 μm band is due to the double contribution of asymmetric stretching ($2\nu_3$) of CO_3^{2-} in carbonates but also due to NH_4-phyllosilicates (Bishop et al., 2002). The ~4.0 μm band is the result of a combination of symmetric and asymmetric stretching ($\nu_1 + \nu_3$) of CO_3^{2-} (Nuevo et al., 2014), which is indicative of carbonates.

Phyllosilicates are globally distributed on Ceres' surface (Ammannito et al., 2016). Variations in the strength of 2.7-μm and 3.1-μm absorption bands are generally correlated, except in Urvara crater, where the abundance of ammoniated phyllosilicates is much more elevated than Mg-phyllosilicates (Ammannito et al., 2016; Longobardo et al., 2018a).

Thermal evolution models (McCord and Sotin, 2005; Castillo-Rogez and McCord, 2010) suggest that Ceres is a carbonaceous chondrite-like body which experienced aqueous alteration, allowing the production of phyllosilicates (Engel et al., 1994) and carbonates (Rivkin et al., 2011). Simulations performed by Neveu et al. (2017) showed that interaction between CM chondritic material and cometary fluid produced, at low temperature, NH_4-bearing minerals, in addition to serpentine, sulphide minerals, magnetite and Mg/Ca-carbonates.

Some localized bright areas, termed "bright spots" (BS) (Palomba et al., 2018) have been widely detected on the Ceres surface. The several brightest BS are located inside Occator crater, on a dome-like formation of 3 km wide (Schenk et al., 2016), i.e., Cerealia Facula, and on its floor, i.e., Vinalia Faculae (De Sanctis et al., 2016; Raponi et al., 2018a). By applying the photometric correction method already validated for Vesta (Longobardo et al., 2014), the Ceres average equigonal albedo, i.e., the radiance factor I/F divided for the disk function and corrected for incidence and emission angles (Longobardo et al., 2018b and references therein), estimated at 1.2 μm under a phase angle of 30°, is about 0.035 (Longobardo et al., 2018b). The brightest areas of Cerealia Facula are characterized by an albedo of at least 5 times the Ceres average (De Sanctis et al., 2016). Spectra of Occator BS are different with respect to the Ceres mean spectrum: the band center of the 2.7-μm absorption is not located at 2.72 μm (as for Ceres average), but at longer wavelengths, at 2.76 μm (De Sanctis et al., 2016); the 3.1-μm spectral feature is very weak in spectra of Occator BS and located at about 3.1 μm, while in Ceres mean spectra the band center of the 3.1-μm feature is at 3.06 μm (Raponi et al., 2018a); the 4.0-μm band center is located toward 4.01 μm, longward with respect to the Ceres mean spectrum, where the band center is located at about 3.96 μm. The composition of Occator Faculae is mainly a mixture of Al-phyllosilicates (illite or montmorillonite), Na-carbonate (natrite), ammoniated salts, and dark material (De Sanctis et al., 2016; Raponi et al., 2018a). New absorption bands are observed at 2.21 and 2.86 μm in Occator BS and secondary absorptions at about 3.2 and 3.3 μm are also present (De Sanctis et al., 2016; Raponi et al., 2018a).

Na-carbonates have been observed in other localized areas of Ceres: in the crater ejecta and floors of Kupalo and Haulani, in small bright exposure in Ikapati crater, in regions corresponding to or close to domes and mounds, such as inside or near Haulani, Oxo, Dantu and Azacca craters (Carrozzo et al., 2018). Spectral features indicative of Na-carbonates are also observed on the flanks of the highest mountain present on Ceres, Ahuna Mons, characterized by an average height of 4 km and 17 km wide (Ruesch et al., 2016; Zambon et al., 2017). On Ceres, mounds and domes are both round-shaped topographic rises, a few or tens of kilometers wide. While the origin of mounds is uncertain, domes (e.g., Occator) can show evidence of flows (Schenk et al., 2016) that could be related to hydrothermal activity (Schenk et al., 2016).

Sodium carbonate is mainly detected in young features (less than 100 s Myr), probably transported to the surface by ascending subsurface liquids or upwelling material from subsurface (Carrozzo et al., 2018).

Organic material has been discovered in the Ernutet crater: on the peak, floor and in the ejecta, but also few kilometers away as in Inamahari and Omonga craters. Spectra of these areas are characterized by a prominent 3.4-μm absorption band, corresponding mainly to the C—H bonds of aliphatic organic compounds (De Sanctis et al., 2017; Vinogradoff et al., 2018). The common 2.7, 3.1- and 4.0-μm spectral features are also present. The organics are therefore mixed with carbonates, Mg-phyllosilicates and NH_4-phyllosilicates.

Spectral absorptions related to H_2O, and located at 1.55 μm and 2.0 μm, have been detected in spectra of Oxo crater, connected with bright material on the wall of crater. Water ice could therefore be present, probably as an icy block or bound up in minerals (Combe et al., 2016; Raponi et al., 2017). Water ice was also discovered in shadowed area of Ceres (Combe et al., 2018; Raponi et al., 2018b), mainly located at higher latitudes, the most favourable places for the preservation of water ice on airless planetary bodies (Platz et al., 2016).

Evolutionary models suggest that Ceres is a differentiated body (Castillo-Rogez, 2011; Travis and Feldman, 2016). Basing on Ceres shape model and gravity field, information about the Cerean internal structure have been constrained (Ermakov et al., 2017): describing Ceres as a two-layer model with uniform density, the crustal density is estimated to be 1287^{-87}_{+70} kg/m^3 and the mantle density is 2434^{-8}_{+5} kg/m^3. Furthermore, an evidence of moderate viscous relaxation is observed on Ceres surface, suggesting that the crust is stronger than a surface composed by water ice (Ermakov et al., 2017). The crustal density obtained is lower than that of rock and combined with a model taking into account viscous relaxation (Ermakov et al., 2017), the resulting composition of volatile-rich crust is likely a mixture of rock, ice, salts and clathrate hydrates (Ermakov et al., 2017), in particular < 25 vol.% water ice, < 36 vol.% phyllosilicates or carbonates and > 29 vol.% hydrated salts or clathrate hydrates (Fu et al., 2017). The thickness of volatile-rich crust is supposed to be 41 km, where at such depth a silicate-rich mantle begins, with a radius of 428. $7^{+4.7}_{-302}$ km (Ermakov et al., 2017).

Liquid water could be buried in the interior of Ceres (Fu et al., 2017; De Sanctis et al., 2016), and the occurrence of ammoniated phyllosilicates on Ceres' surface could suggest the presence of ammonia in the subsurface, a compound that lowers the freezing point of water and which would allow the liquid phase of water to exist at depth (De Sanctis et al., 2016).

The mineralogical composition of the subsurface can be investigated by studying the central peak of complex craters on Ceres' surface, raised from the subsurface as a consequence of an impact event. Material composing the central uplift is termed crater central peak material (ccp): given its central location within the impact crater, it is probably minimally mixed by the material falling from the crater walls.

The spectral investigation of ccps was undertaken here to provide insights into the mineralogical composition of Ceres' subsurface and detect possible variations with respect to the outer layer of crust, and as a function of excavation depth and latitude. In particular, spectral parameter as band center and band depth are relevant to mineralogically investigate ccp. The band center of absorption bands provides information about the identity of minerals, while the depth of bands

can provide a preliminary evaluation of minerals' abundance. For example, spectra of Mg/Ca-carbonates (the most diffused carbonate on Ceres' surface), such as calcite, dolomite and magnesite (acquired from the RELAB database and characterized by a grain size of 0–45 μm), have a band center of 4.0-μm absorption bands at 3.979 μm, 3.958 μm and 3.943 μm, respectively. The spectrum of a Na-carbonate (natrite; which is part of Occator Faculae's composition) is characterized by a band center at 4.011 μm (in the case of a sample with a grain size of 0–45 μm). At shorter wavelengths, most of the spectra of Ceres surface have a band center at 2.72 μm, suggesting the occurrence of Mg-phyllosilicates, while the position at 2.76 μm in Occator Faculae is indicative of Al-phyllosilicates. The IR spectral slope, estimated between 1.2 and 1.9 μm, could be a good marker of space weathering or changing composition/grain size.

In Section 2, VIR data used to perform the mineralogical analysis are described. In Section 3, a detailed description about the formation of complex craters and the nature of ccp is provided. The procedure to select Ceres ccps is described in Section 4, in addition to the method used to retrieve both spectral parameters of ccps and depths of excavation of craters, subsurface areas from where ccps emerged. The statistical method is also described in Section 4, which is used to strengthen the results obtained by spectral analysis, which are shown in Section 5. Results are discussed in Section 6 and conclusions are provided in Section 7.

2. VIR dataset

The VIR spectral range spans from the near UV to the near IR, i.e., from 0.25 to 5.1 μm. In particular, two data channels are combined to obtain the entire spectral range, the visible channel, that covers the 0.25–1.05-μm range (sampling of 1.8 nm) and the infrared channel, which extends from 1.05 μm to 5.1 μm (sampling 9.8 nm) (De Sanctis et al., 2011). In the entire VIR dataset, spectral artifacts have been removed (Carrozzo et al., 2016). Furthermore, the thermal contribution in VIR spectra has been modeled and removed (Raponi et al., 2017; Raponi et al., 2018a), in order to obtain thermally corrected reflectance spectra.

The Dawn mission was divided into different phases on the basis of the spacecraft altitude: Approach, Rotation Characterization (RC) (before gravitational capture and orbiting of Dawn around Ceres), Survey, High-Altitude Mapping Orbit (HAMO) and Low-Altitude Mapping Orbit (LAMO). The HAMO phase orbit took place from August 17th to October 23rd, 2015, with a spacecraft altitude of 1470 km. The LAMO mission phase acquired data from December 16th, 2015 to September 2nd, 2016 when the spacecraft was at the minimum altitude of 385 km. In this study we used the HAMO and LAMO datasets, which provided hyperspectral images with high spatial resolution, i.e., 360–400 m/pixel and 90–110 m/pixel, respectively.

3. Science background

Complex craters are significant impact structures characterized by a flat floor, an inward collapse around the rim, and a central uplift (Dence, 1968; Grieve, 1991). The formation of complex and simple craters (bowl-shaped) involves three stages: the contact/compression stage, the excavation stage, and the modification stage. The first stage occurs when the projectile makes contact with the surface of the target, releasing kinetic energy by shock waves, generated at the interface between projectile and target (Kieffer and Simonds, 1980; O'Keefe and Ahrens, 1982, 1993; Melosh, 1989). Shock waves propagate into a larger hemispherical area with increasing distance from the impact point, progressively reducing the shock energy and pressure. The interaction of shock waves with the target rock causes the material in the upper level to move upward and outward (creating ejecta and crater rim), while target material at lower levels is pushed downward and outward. As a result, in this excavation stage, a bowl-shaped depression, i.e., the transient cavity, is produced (Maxwell, 1977; Grieve et al., 1977; Melosh, 1989). The final configuration of the impact depression occurs in the modification stage, in which, on the basis of size, structure and properties of target rock, a simple or complex crater is formed. Simple craters are small structures that do not substantially modify the original shape of a transient cavity. Complex craters form when a large impact event releases enough energy to overcome the fundamental strength of a large volume of rock beneath the transient cavity. Consequently, during the modification stage, complex interactions between shock-wave effects, gravity and rock properties occur and produce outward, inward and upward movements of large volumes of the material below the crater. As a general result, an "elastic rebound" occurs and a volume of rock beneath the central part of the transient cavity rises to form a central uplift (Dence, 1968; Grieve et al., 1981), within a timespan of a few minutes (Melosh, 1989). On Ceres, complex craters with central peaks form when the minimum crater diameter is about 25 km, consistent with an ice-bearing upper crust (Hiesinger et al., 2016).

In order to indicate the material forming the central uplift, we use the term "crater central peak material (ccp)" in accordance with the same nomenclature used in the geological map of Ceres (Mest et al., 2018; Williams, 2018). On Ceres, ccps have been observed as a cone (in the case of Kondos crater) or as mountainous ridges with a rough surface (Haulani crater), characterized by steep slope angles and a low crater density (Krohn et al., 2017), as can be observed in Fig. 2 of following chapter. Since ccp are located in the center of crater, they are probably isolated from mass wasting along the crater walls, which could cause mixing.

Given the characteristics of crater central peak material, the spectral analysis of this geologic feature could be useful to investigate the mineralogical composition of Ceres' subsurface and to detect possible variations with respect to the surface.

4. Tools

4.1. Data selection

Ccps analyzed in this work were selected using the following procedure: 1) craters with a central peak, marked in geological maps of Ceres, were selected (i.e., Mest et al., 2018); 2) a square-shaped area was defined around each peak, scaled with the size of peak in order to surround the highest topographic zone, and sides of square were defined with minimum and maximum value of both latitude and longitude (Fig. 2); 3) the VIR dataset covering the selected area was analyzed. Since the area of each peak is very limited, only reflectance spectra with high spatial resolution were considered, i.e., HAMO and LAMO data. Finally, a catalogue of 32 ccps (a minor number than those marked in geological maps) was compiled and their spatial distribution can be observed in Fig. 1, marked by magenta dots.

Properties of the 32 ccps are summarized in Table 1. In particular, ccps are listed in order of decreasing latitude. For unknown craters, we used a progressive number after the term "CCP". 22 ccps are in the northern hemisphere and 10 ccps are localized in the southern hemisphere. The smallest crater with a central peak is Nepen, crater diameter of 26.4 km, while Urvara is the largest crater characterized by a crater diameter of 170 km. Taking into account the age obtained from the Lunar-Derived Absolute Model Age (LDM; Hiesinger et al., 2016; Schmedemann et al., 2014), Haulani, Occator, Tupo, Kokopelli, Azacca, Ikapati, Victa and Abellio are young features, with ages less than 80 Myr (million years); Fejokoo and Dantu formed in an intermediate age, i.e., between 80 and 180 Myr ago; and Datan, Urvara, Ninsar, Sintana, Achita, CCP8, Omonga and Ernutet are older features because their formation age is more than 200 Myr (Stephan et al., 2018). The Asteroid-Derived Absolute Model (Hiesinger et al., 2016; O'Brien et al.,

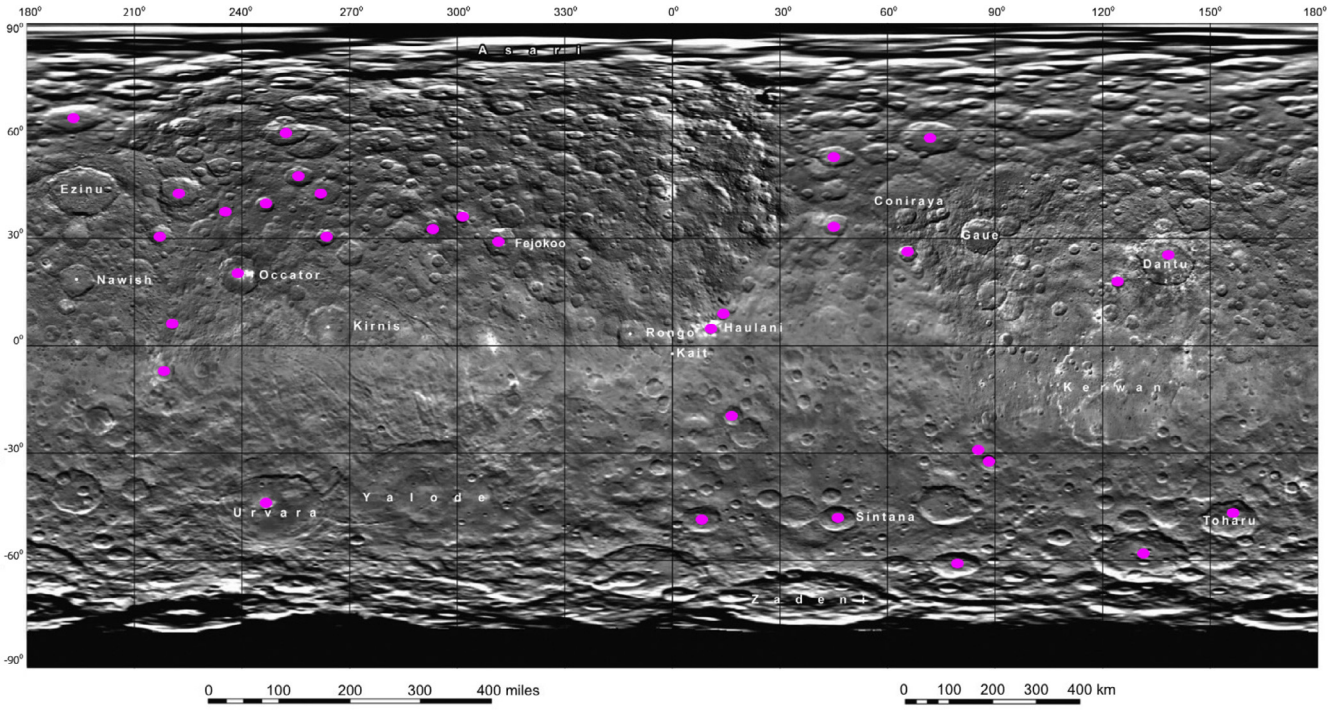

Fig. 1. Distribution of the 32 ccps analyzed in this work (magenta dots) superimposed on the Framing Camera mosaic of Ceres (courtesy FC Team). (For interpretation of the references to colour in this figure legend, the reader is referred to the web version of this article.)

Table 1
List of ccps considered in this work. The columns report: the quadrangle where each ccp is located; the name of the ccp; the diameter (expressed in km) of the crater containing the central peak; the age of the crater's formation estimated following the Lunar-Derived Absolute Model Age (LDM, express in Myr); coordinates that define the area of the central peak, i.e., minimum and maximum latitude, minimum and maximum longitude.

Quadrangle	Name	Diameter (km)	LDM (Myr)	Min/Max latitude	Min/Max longitude
Ezinu	CCP1			62,8 °N/64,23 °N	192 °E/196 °E
Ezinu	Datan	60 [a]	213 + /−9,9 [1]	59,5 °N/60 °N	250,8 °E /253 °E
Coniraya	Omonga	77 [a]	970 + /−70 [2]	57,63 °N /58,83 °N	70,02 °E /74,35 °E
Coniraya	Ernutet	53,4 [a]	1600 + /−200 [2]	52,07 °N /53,6 °N	43,9 °E /46,2 °E
Ezinu	CCP5			46,76 °N /48,34 °N	254,9 °E /256,8 °E
Ezinu	Kaikara	72 [a]		41,48 °N /43,77 °N	221,8 °E /224,47 °E
Ezinu	CCP7			41,4 °N /42,05 °N	261,5 °E /262,2 °E
Ezinu	CCP8		906 + /−130 [1]	38,6 °N /40,77 °N	245,7 °E /247,5 °E
Ezinu	CCP9			36,65 °N /37,09 °N	234,56 °E /235,49 °E
Fejokoo	Victa	32 [a]	<80 [3]	35,6 °N /36,3 °N	301,2 °E /302,16 °E
Coniraya	Ikapati	50 [a]	71 + /−5 [2]	32,9 °N /34,3 °N	44,2 °E /46,2 °E
Fejokoo	Abellio	32 [a]	<80 [3]	32,6 °N /33,7 °N	292,8 °E /293,5 °E
Ezinu	CCP13			30,5 °N /31,64 °N	216,04 °E /217,5 °E
Ezinu	Ninsar	40 [a]	378 + /−33 [1]	29 °N /30,6 °N	262,6 °E /264,5 °E
Fejokoo	Fejokoo	68 [a]	80–180 [3]	28 °N /30 °N	310 °E /312,7 °E
Coniraya	Achita	40 [a]	570 + /−60 [2]	25,03 °N /26,5 °N	65,27 °E /66,3 °E
Dantu	Dantu	126 [a]	111 + /−39 [4]	23,46 °N /26 °N	136,88 °E /140,18 °E
Occator	Occator	92 [a]	34 + /−2 [5]	19,11 °N /20,13 °N	237,49 °E /238,61 °E
Kerwan	Kokopelli	30.7 [b]	41.67 + /−2.14 [6]	17,35 °N /18,87 °N	124 °E /125,4 °E
Haulani	CCP20			8,06 °N /9,06 °N	13,9 °E /14,4 °E
Occator	Nepen	26.4 [a]		5,89 °N /6,47 °N	220,1 °E /221,14 °E
Haulani	Haulani	34 [a]	2,7 + /−0,7 [7]	5,37 °N /6,24 °N	10,05 °E /11,41 °E
Occator	Azacca	49,91 [a]	75,9 + /−15 [7]	6,95 °S /6 °S	217,73 °E /219,35 °E
Haulani	Kondos	44 [a]		20,19 °S /19,11 °S	16 °E /17,8 °E
Sintana	CCP25			29,15 °S /28,39 °S	85,02 °E /85,77 °E
Sintana	Tupo	36 [a]	29 [6]	32,57 °S /31,4 °S	87,37 °E /88,8 °E
Urvara	Urvara	170 [a]	242 + /−16 [7]	46,05 °S /43,24 °S	244,51 °E /250,31 °E
Sintana	Annona	60 [a]		48,94 °S /47 °S	7,21 °E /9,89 °E
Toharu	Toharu	86 [a]		49,4 °S/47,4 °S	154,3 °E /159,2 °E
Sintana	Sintana	58 [a]	390 + /−30 [8]	49,61 °S /48,29 °S	46,07 °E /47 °E
Toharu	Chaminuka	122 [a]		59,41 °S /57,66 °S	130,43 °E /132,01 °E
Sintana	Hamori	60 [a]		61,3 °S /60,2 °S	77,04 °E /81,06 °E

References for LDM: [1], Scully et al., 2017; [2], Pasckert et al., 2017; [3], Hughson et al., 2017; [4], Kneissl et al., 2016; [5], Nathues et al., 2015; [6], Personal Communication; [7], Schmedemann et al., 2016; [8], Schulzeck et al., 2017.
References for diameter values: [a], Anon1; [b], Personal Communication.

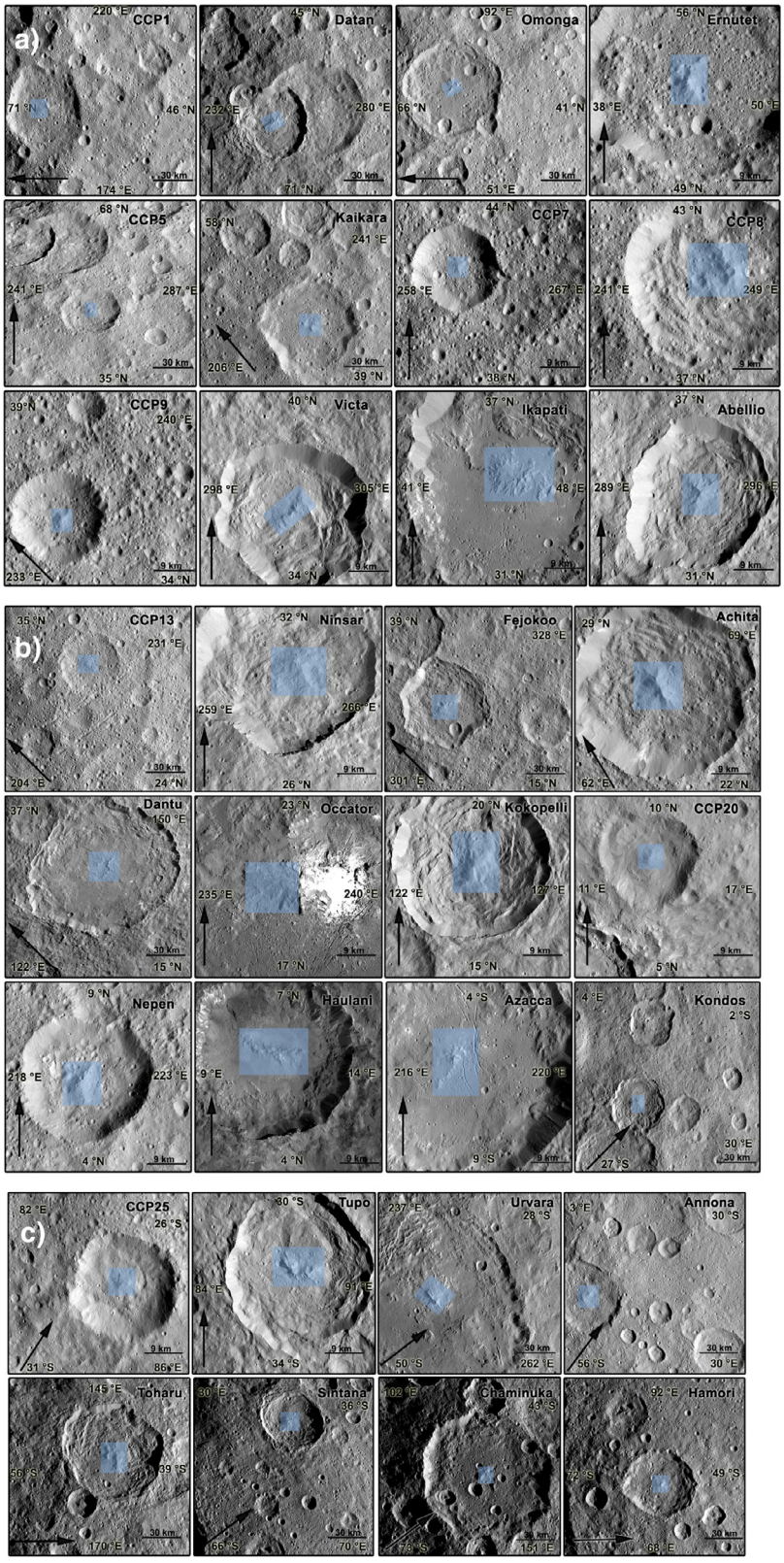

Fig. 2. a), b) and c) Images of spectrally analyzed ccps, acquired by the Framing Camera on board Dawn. The spectrally analyzed square-shaped area around each ccp is marked in light blue color. Black arrow indicates the North. Some images were acquired during the HAMO phase and are characterized by a resolution of about 139 m/pixel (a scale of 30 km is shown), whereas other ones were acquired during the LAMO phase and their resolution is about 38 m/pixel (a scale of 9 km is shown). Furthermore, for each image, the minimum and maximum latitude and longitude is specified. (For interpretation of the references to colour in this figure legend, the reader is referred to the web version of this article.)

2014) provides different absolute ages, but the relative ages among craters are preserved. However, since the LDM provided the age for a greater number of crater with respect to the ADM, we used the former in our work. Images of studied ccps are in Fig. 2, where the spectrally investigated area, for each ccp, is marked by light blue color.

4.2. Spectral parameters and photometric correction

Mineralogical analysis was performed by comparing different parameters retrieved in the reflectance spectra, such as band center (BC) and band depth (BD) of absorption bands and spectral slope. In

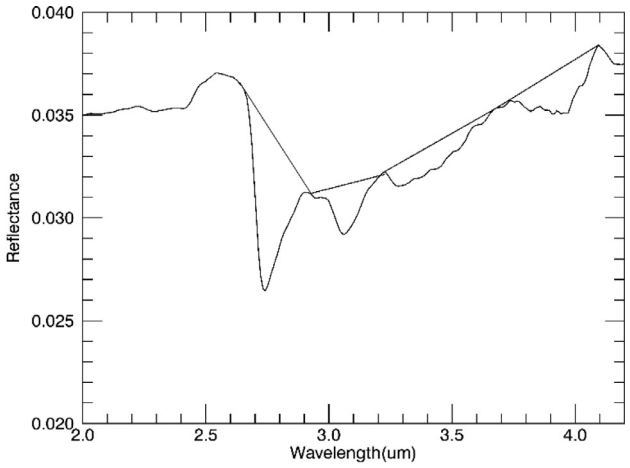

Fig. 3. Reflectance spectrum of Ceres, belonging to a region characterized by mean value of reflectance, where the spectral continuum is fitted by straight lines, one for each absorption band.

particular, we considered band centers and band depths of the 2.7-, 3.1-, 3.4- and 4.0-μm absorption bands, in addition to the spectral slope.

To retrieve band centers and band depths in Cerean reflectance spectra, a continuum across each band was removed, by applying the linear continuum method described by Galiano et al. (2018). In particular, the method fits the spectral continuum with straight lines, one for each absorption band, whose endpoints are located on the band shoulders (Fig. 3). It can be used to account for the different band shapes observed in spectra of particular areas, especially in Cerealia and Vinalia Faculae.

The band center is the wavelength corresponding to the minimum reflectance value in the isolated absorption bands, after removal of continuum. The band depth is obtained as $1 - R_b/R_c$, where R_b is the reflectance at the band center and R_c is the corresponding reflectance of the continuum (Clark and Roush, 1984). The 3.1- μm and 3.4-μm absorption bands, in ccps reflectance spectra, were fitted by second order polynomial curves; therefore, the band center in these bands is the wavelength with the minimum fitted value. For each ccp, spectral slope, band center, and band depths of 2.7-, 3.1- and 3.4-μm bands were estimated for each single reflectance spectrum included in the selected area: mean values and their standard deviations are consequently computed.

A different procedure was applied to obtain spectral parameters of the 4.0-μm region absorption band. The method applied to remove the thermal contribution (Raponi et al., 2017) could introduce some noise in the estimation of 4.0-μm band depth because of the error associated to the level of spectral continuum after the thermal removal (for the definition of band depth): the level of spectral continuum longward of 3 μm is the result of the fitted spectral reflectance and the thermal contribution. The latter could be overestimated or underestimated in the fitting procedure, thus altering the level of spectral continuum once the thermal emission is removed. A suitable test demonstrated that the noise of the spectral continuum (after thermal removal) shortward and longward 3 μm is comparable. In particular, areas of Ceres surface, composed of the same mineralogy, were compared, and the reflectance both at 1.2 μm and at 3.65 μm was estimated: the standard deviation of both reflectances in these areas is very low, less than 0.2%, suggesting that the thermal removal does not add any significant noise to the estimation of the 4.0-μm band depth. Some signal fluctuations can, however, affect analysis of the absorption band located at about 4 μm, due to the low signal-to-noise ratio. Since no polynomial curves are suitable to fit this spectral feature well, we used the mean spectrum for each ccp to determine band center and band depth of 4.0-μm spectral feature.

Band depths values of 2.7-, 3.1- and 3.4-μm spectral features in ccp spectra are affected by photometrical effects, therefore an appropriate correction was performed and photometrically corrected values relative to a phase angle of 0° were retrieved, following the method by Longobardo et al. (2018b). The method consists the retrieval of an empirical relation between band depth and phase angle, based on a statistical analysis. According to the assumption that reflectance is the product of a disk function (depending on observation geometry, only) and a phase function (depending on phase angle and wavelength), band depths are independent of incidence and emission angles. The relation between band depths and phase angle has been instead retrieved by considering median values of band depth in each phase angle bin (1° width). The linear relation obtained between these band depth values and phase angle has been then used to extrapolate the band depth at 0° (Longobardo et al., 2018b).

4.3. Estimation of ccp's pseudo-depth

In addition to spectral parameters and estimated ages (LDM) of ccps, we considered other parameters to better characterize the subsurface composition, in particular the local radius of each crater and its depth. The local radius is the distance between the Ceres surface and its center of mass, estimated by using Ceres' shape model: we considered the local radius relative to the maximum altitude of peaks (lr_p).

The dwarf planet has an ellipsoidal shape with mean dimensions of axes a, b and c respectively of 965.2 ± 2 km, 961.2 ± 2 km and 891.2 ± 2 km (Russell et al., 2015). We calculated, for each ccp the coordinates (x, y and z) of the highest part of the central uplift on the ellipsoid, by using the parametric expressions:

$$\begin{cases} x = \frac{a}{2} cos\varphi cos\vartheta \\ y = \frac{b}{2} cos\varphi sin\vartheta \\ z = \frac{c}{2} sin\varphi \end{cases}$$

where φ and θ are respectively the latitude and longitude of the highest part of the central uplift. Consequently, the distance between the maximum height of the central peak and the center of the ellipsoid, referred to as e_p, is obtained as $\sqrt{x^2 + y^2 + z^2}$. The difference between the local radius of the central peak (lr_p) and the ellipsoidal surface (e_p) provides the elevation of peak with respect to the ellipsoid. The same method applied to the entire Ceres surface provides the Ceres topographical map (Fig. 4), a map in accordance with the topographic map produced by JPL and DLR (Anon2).

The material composing the central peak is uplifted from its original depth during the modification stage of crater formation and this stratigraphic uplift (s_u) is a function of the final crater diameter (d), estimated to be about $0.1d$ for terrestrial complex craters (Grieve et al., 1981; Ivanov et al., 1982; Grieve and Pilkington, 1996). This relationship has been applied to various planetary surfaces to investigate the mineralogy of the subsurface, as for the Moon (Pinet et al., 1993; Pieters et al., 1997) and Mars (Tornabene et al., 2008; Baratoux et al., 2007; Pan et al., 2015). We applied such relationship also on Ceres, even if uncertainties could be present for different rheologies of Cerean crust with respect to terrestrial, lunar and martian crust. The aim is, by using such relationship, to obtain preliminary information about the subsurface mineralogy and to compare craters of different sizes and excavation depths. Therefore, the "pseudo-depth" of material composing the central uplift is obtained by removing the stratigraphic uplift of peak from its elevation with respect to the ellipsoid:

$$\text{Pseudo} - \text{depth} = (lr_p - e_p) - 0.1d$$

We also estimated the error associated to the pseudo-depth, by propagating the error on the x, y and z axis, that are:

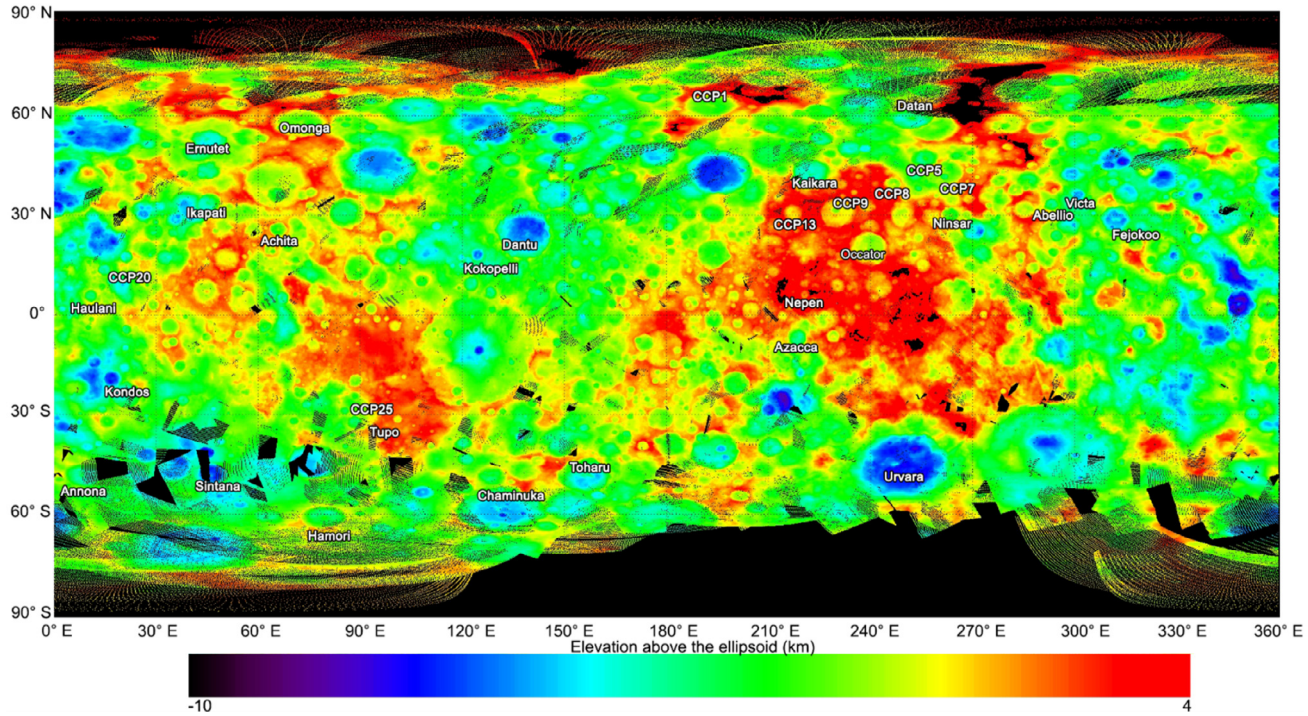

Fig. 4. Topographic map of Ceres obtained from the difference between the local radius and the relative position on the ellipsoidal surface for each VIR pixel. Colors in the map correspond to the different heights of geographical features with respect to the ellipsoid: violet indicates the deepest depressions, whereas red areas are indicative of topographic highs. (For interpretation of the references to colour in this figure legend, the reader is referred to the web version of this article.)

$$\begin{cases} \sigma_x = \frac{\sigma_a}{2} cos\varphi cos\vartheta \\ \sigma_y = \frac{\sigma_b}{2} cos\varphi sin\vartheta \\ \sigma_z = \frac{\sigma_c}{2} sin\varphi \end{cases},$$

where σ_a, σ_b and σ_c are 2 km (Russell et al., 2015).

In particular, the error σ of a function f (x,y,z) is, by following the general expression:

$$\sigma = \sqrt{\left(\frac{\partial f}{\partial x}\right)^2 \sigma_x^2 + \left(\frac{\partial f}{\partial y}\right)^2 \sigma_y^2 + \left(\frac{\partial f}{\partial z}\right)^2 \sigma_z^2},$$

Since lr_p and d are assumed to be free by error, the error on the pseudo-depth ($\sigma_{p.-d.}$) is coincident with the error on e_p, i.e.:

$$\sigma_{p.-d.} = \sigma_e = \sqrt{\frac{x^2\sigma_x^2 + y^2\sigma_y^2 + z^2\sigma_z^2}{x^2 + y^2 + z^2}}$$

In Extended data 2, for each ccp, the crater diameter, the depth of the central peak with respect to the ellipsoid (lr_p-e_p), the pseudo-depth (p.-d.) and the error connected to the pseudo-depth ($\sigma_{p.-d.}$) are reported.

4.4. Statistical analysis: Pearson and bootstrap

We used the Pearson correlation coefficient (PCC) to define the relationship between different spectral parameters and to better constrain the mineralogical composition of ccps. The Pearson coefficient estimates a linear correlation between two variables, X and Y, by considering the covariance of variables (cov(X,Y)) and their standard deviations (σ_X and σ_Y). In particular, the Pearson coefficient is defined as $\frac{cov(X,Y)}{\sigma_X \cdot \sigma_Y}$. The resulting value is between -1 and 1, suggesting an anti-correlation and a linear correlation, respectively. If the Pearson value is included between 0 and 0.3, the correlation is weak; for values between 0.3 and 0.7 the correlation is moderate; and a strong correlation is obtained for values greater than 0.7. A Pearson coefficient close to 0 suggests the absence of any link between parameters.

Since spectral parameters obtained in our work are mean values with standard deviations (except for the 4.0-μm spectral feature, where the band center and band depth are obtained by the mean spectrum of ccp, see table in Extended data 1), we estimated the Pearson coefficient following a more meticulous approach. For example, to estimate the possible correlation between the 2.7- and 3.1-μm band depths (for simplicity, we use the expression 2.7BD and 3.1BD), we used the following method which included their standard deviations:

- the values of 2.7BD and 3.1BD, for each ccp, have been randomly chosen between their minimum and maximum value of standard deviation, i.e., between 2.7BD-2.7SD and 2.7BD + 2.7SD (for the 2.7BD) and between 3.1BD-3.1SD and 3.1BD + 3.1SD (for the 3.1BD);
- 32 random values of both 2.7BD and 3.1BD were obtained (one for each ccp);
- the Pearson coefficient between the two groups of parameters was estimated;
- the procedure was repeated 500 times in order to consider various combinations;
- the mean value of Pearson, estimated among the 500 Pearson values, was obtained with its relative standard deviation.

The Pearson coefficient obtained with such a procedure considers the deviations from each single mean value, producing a more accurate result than the Pearson coefficient estimated only on the mean values. The above described procedure cannot be applied if the standard deviation of one or both the two variables is not known, therefore, when the statistical analysis involves the 4.0-μm band depth, a SD corresponding to 0 is assumed for this spectral parameter. To avoid confusion, we refer to the Pearson-SD coefficient (abbreviated P-SD) when the coefficient is estimated by applying the above described procedure. In the Extended data 3, each coefficient estimated in this work is reported.

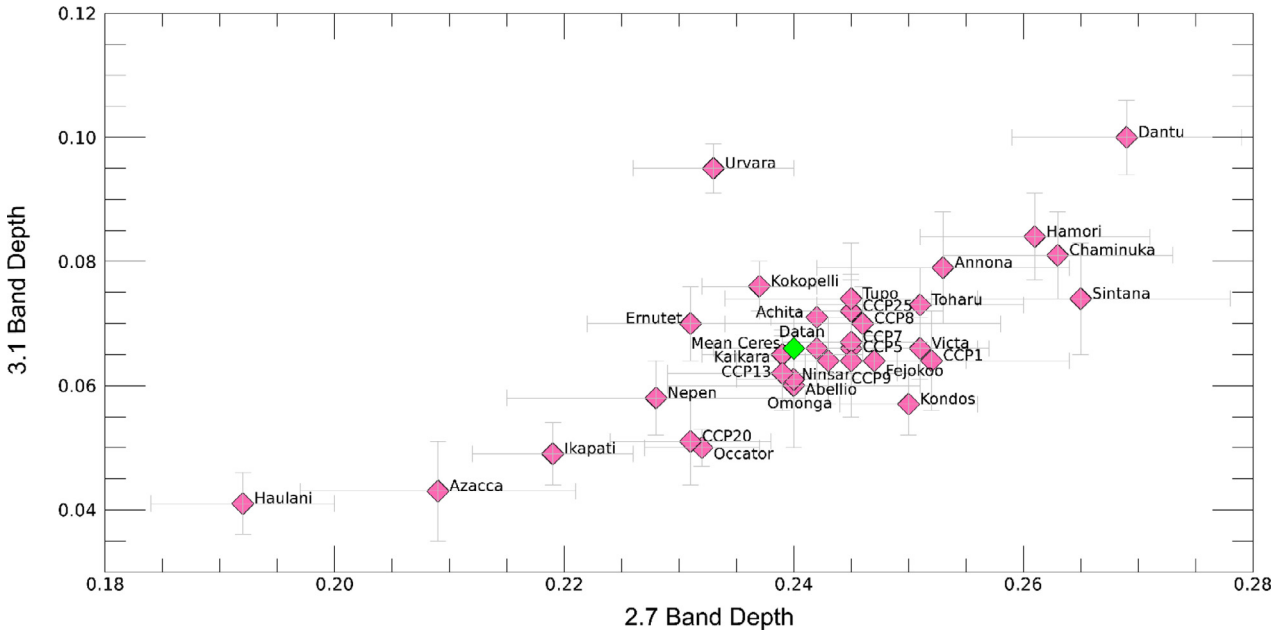

Fig. 5. Scatterplot of 2.7-μm band depths vs 3.1-μm band depths (grey bars represent standard deviations) for Cerean ccps (magenta diamonds). The mean Ceres value (green diamond) is also shown for comparison. (For interpretation of the references to colour in this figure legend, the reader is referred to the web version of this article.)

5. Analysis of ccps' parameters

5.1. Mg-phyllosilicates vs NH_4-phyllosilicates

In Fig. 5, the scatterplot of 2.7-μm band depths (relative to Mg-phyllosilicates) vs 3.1-μm band depths (due to NH_4-phyllosilicates) of ccps is shown. As observed for the entire Ceres surface (Ammannito et al., 2016), as well as on the ccps, Mg-phyllosilicates and NH4-phyllosilicates are correlated. The value relative to the mean Ceres surface (green diamond) is also shown in the scatterplot for comparison. A moderate correlation between 2.7 μm band depths and 3.1 μm band depths of ccps is observed (P-SD coefficient is 0.66 ± 0.02). Haulani ccp is the most depleted in phyllosilicates, while Dantu ccp is characterized by the highest abundance of Mg- and NH_4-phyllosilicates. In Fig. 6, a three-dimensional representation of the Dantu crater is shown. In Fig. 6a, the 2.7-μm band depth is mapped on the Dantu surface, while the 3.1-μm band depth is mapped in Fig. 6b: both absorption bands are generally deeper on the peak, suggesting a higher concentration of phyllosilicates in the central uplift.

Urvara ccp falls off this trend: the 2.7-μm band depth is similar to the value of the mean Cerean surface, while the 3.1-μm band depth is very deep, implying an abundance of NH_4-phyllosilicates comparable to that of Dantu, i.e., an excess of ammonium.

5.2. Carbonates scatterplot

The 3.4- and 4.0-μm band depths are mainly associated with Mg/Ca-carbonates (De Sanctis et al., 2015) even though NH_4-phyllosilicates also have a broad band at 3.4 μm (Bishop et al., 2002), contributing to the Ceres band. The scatterplot of these two bands can be observed in Fig. 7, characterized by a P-SD coefficient of 0.47 ± 0.03, suggesting that the two bands are related, as expected, since they are mainly associated to the same minerals, i.e., carbonates. The largest number of ccps are clustered in a range of values of 4.0-μm band depth of 0.046 to 0.06. This cluster is limited to a region where the minimum value for the 3.4-μm band depth is 0.02 and the maximum value is 0.045. Some ccps show atypical band depth values and plot out of the cluster (marked by red ellipses). These are cases of: (1) weak 3.4-μm absorption bands and strong 4.0-μm bands (Abellio, CCP25, Haulani and Ikapati), (2) strong 3.4-μm band depths and weak 4.0-μm band depths (Sintana), and (3) high 3.4- and 4.0-μm band depth values (Chaminuka, Ernutet, Urvara). The exclusion of these ccps from the estimation of the P-SD coefficient produces a value of 0.58 ± 0.05, preserving the moderate correlation between the carbonate bands. The ccps that show anomalous values in the carbonates scatterplot are likely due to the presence of other compounds (such as organics or Na-carbonates) or to elevated abundance of most common minerals (such as ammoniated minerals) that could change depth and shape of one or both of the 3.4- and 4.0-μm bands.

Haulani, Ikapati, Urvara, Ernutet ccp and CCP25 are characterized by the strongest mean values of 4.0-μm band depth. In these particular cases, band center and band depth values were carefully analyzed for each VIR pixel included in the area of ccp. Furthermore, different reflectance spectra of both dolomite (Mg/Ca-carbonate) and calcite (Ca-carbonate), with a grain size of 0–45 μm (analogue to grain size of carbonates on Ceres' surface (De Sanctis et al., 2015)), were acquired from the RELAB spectral database, deconvolved to the VIR spectral sampling, and their 4.0-μm band center was determined. The same procedure was performed on reflectance spectra of natrite (Na-carbonate) with grain size between 0 and 45 μm and obtained at HOSERLab. As result, the 4.0-μm band center of dolomite is found to be between 3.944 and 3.963 μm, the 4.0-μm band center for calcite varies between 3.963 and 3.982 μm, and the 4.0-μm band center for natrite ranges from 3.990 to 4.010 μm.

The analysis of the 4.0-μm band center position for each ccp suggests the presence of Na-carbonates in the Ikapati (Fig. 8), Haulani (Fig. 9) and Ernutet ccps (Fig. 10), mixed with Mg/Ca-carbonates. In particular, reflectance spectra of ccps with a 4.0-μm band center between 3.944 and 3.955 μm are consistent with the occurrence of dolomite as a carbonatic component, while calcite could compose the areas of ccps with 4.0-μm band center between 3.972 and 3.982 μm; pixels with a band center at 3.963 μm suggest a mixture of calcite and dolomite. Reflectance spectra of ccps with a band center between 3.990 and 4.010 μm are indicative of Na-carbonate (as natrite), responsible for the shift toward longer wavelength of the 4.0 μm band center. Furthermore, pixels with a 4.0-μm band center position between about 3.98 and 3.99 μm could indicate a mixture of calcite and natrite. However, it is likely that a reduced abundance of Na-carbonate also occurs in

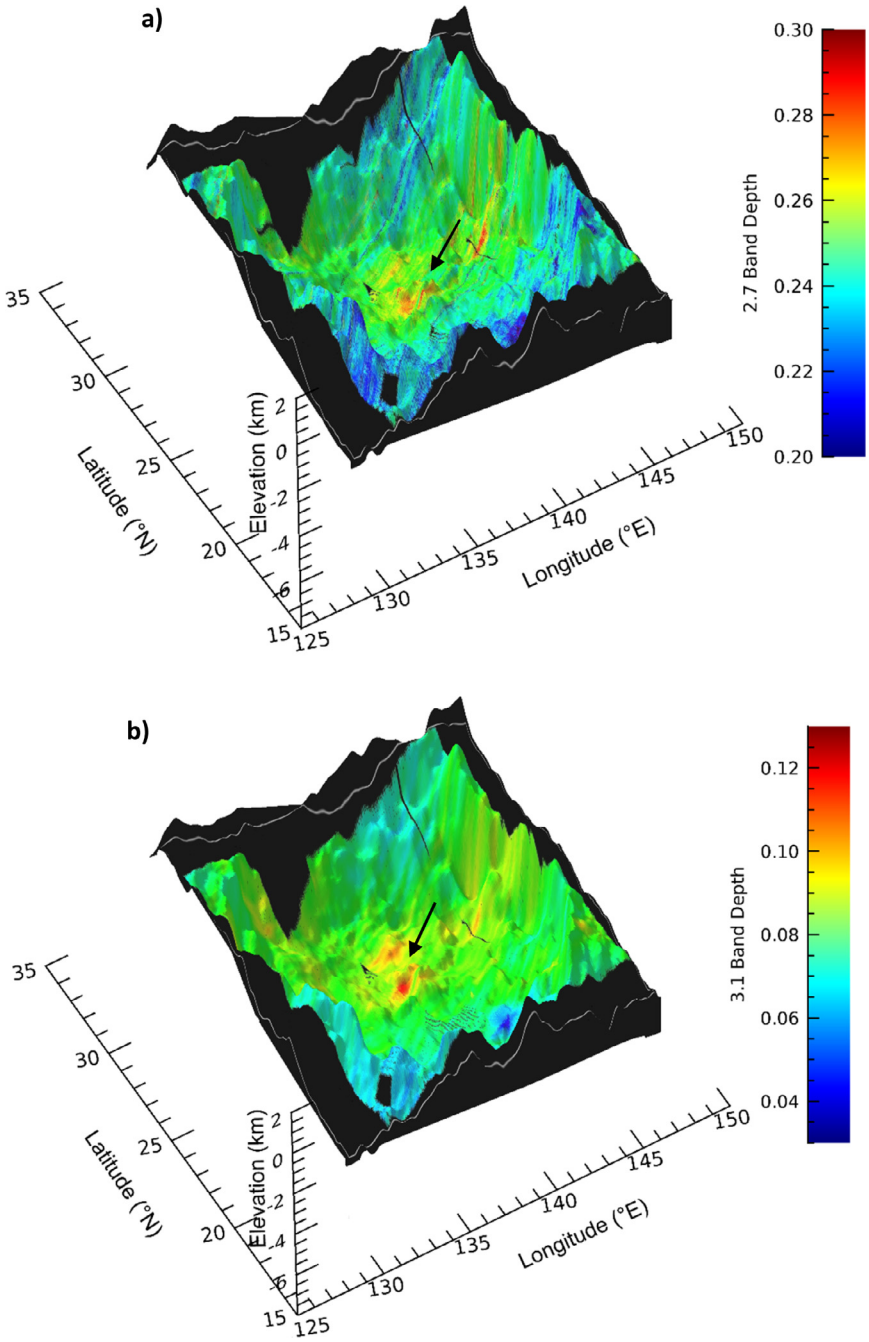

Fig. 6. Three-dimensional representation of Dantu crater onto which the map of 2.7-μm band depth (a) and the 3.1-μm band depth (b) has been superimposed. The highest abundance of both Mg-phyllosilicates and NH_4-phyllosilicates are mainly observed on the peak (denoted by the black arrow). Latitude and longitude are respectively on the y- and x-axis, and the elevation of surface with respect to the ellipsoid (i.e., the difference between the local radius of the central peak (lr_p) and the ellipsoidal surface (e_p), which allowed us to reproduce the Cerean topographical map) is shown on the z-axis. As can be observed in the *Extended data 2*, the elevation of Dantu's peak with respect to the ellipsoid is about −2.6 km, whereas rims are the highest part of crater, with an elevation of about 2 km.

reflectance spectra with the 4.0-μm band center located shortward of 3.99 μm.

In conclusion, the main carbonatic component in the largest number of ccps is the Mg/Ca-carbonate, since the maximum value of the 4.0-μm band center is at 3.99 μm, whereas Haulani, Ikapati and Ernutet ccps are clearly composed of a mixture of Na-carbonates and Mg/Ca-carbonates.

The 3.4- and 4.0-μm band depths moderately correlate (Pearson value of 0.54) in Ernutet's ccp. In particular, the correlation occurs when Na-carbonates, responsible for increasing the 4.0-μm band depth, and organics, responsible for the 3.4-μm band depth, coexist (see also Raponi et al., 2017), as shown in Fig. 11.

The Urvara, Sintana, Abellio ccp and CCP25 are mainly composed of Mg/Ca-carbonates. The Urvara ccp is the peak with the deepest 3.4-μm band depth, in addition to a large 3.1-μm band depth.

5.3. Carbonates vs phyllosilicates

In the scatterplot of 3.4- vs 4.0-μm band depths some peculiar ccps are observed, which are out of the main cluster. Excluding these peculiar ccps (Ikapati, Haulani, Abellio, Sintana, Ernutet, Chaminuka, Urvara and CCP25), a weakly moderate correlation is shown between the 4.0-μm and the 2.7-μm band depths (Fig. 12), and between the 4.0-μm and the 3.1-μm band depths (Fig. 13). In particular, the 4.0-μm band depths are correlated to the 2.7-μm band depths with a P-SD coefficient of 0.38 ± 0.002, while the 4.0-μm band depths are correlated with the 3.1-μm band depths with a P-SD value of 0.3 ± 0.02. If peculiar ccps are included in the estimation of the P-SD coefficient, the 2.7- and 4.0-μm band depths are anti-correlated (with a value of − 0.33 ± 0.02) and the 3.1- vs 4.0-μm band depths are not correlated (with a value of 0.06 ± 0.02). The different trend that emerges in the

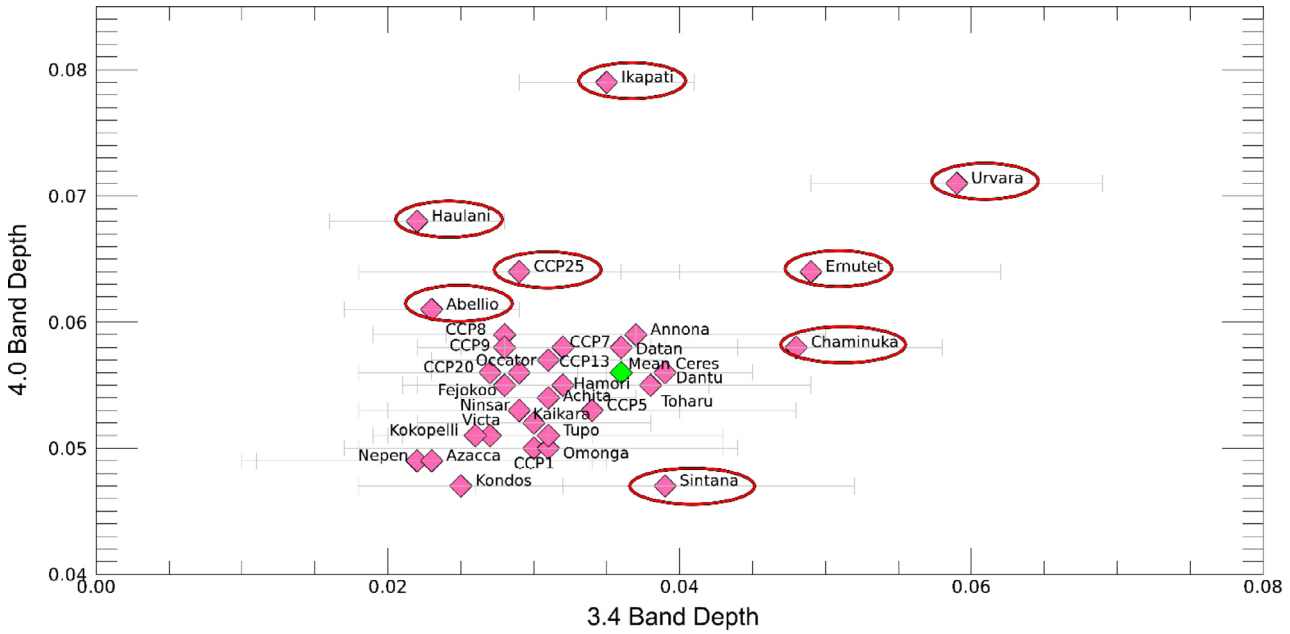

Fig. 7. Scatterplot of 3.4-μm band depths vs 4.0-μm band depths for Ceres ccps (magenta diamonds). The mean Ceres value (green diamond) is also shown for comparison. Peculiar ccps are marked by red ellipses and grey bar represents standard deviation of 3.4-μm band depth. (For interpretation of the references to colour in this figure legend, the reader is referred to the web version of this article.)

scatterplot of the 2.7- vs 4.0-μm band depths, when the peculiar ccp are included (anti-correlation), is likely due to Haulani and Ikapati. Due to the relatively younger formation age, these craters are poorer in Mg-phyllosilicates (Stephan et al., 2018) and richer in Na-carbonates, as observed in the previous sub-section.

From the relationships of 3.4-μm band depths with both Mg-phyllosilicates and NH_4-phyllosilicates, several important correlations emerge. The P-SD coefficient for the scatterplot of 3.4- vs 2.7-μm band depths (Fig. 14) is moderate (0.41 ± 0.04) if the Urvara and Ernutet ccps are excluded, while a stronger correlation (P-SD of 0.63 ± 0.03) is obtained for the scatterplot of the 3.4- vs 3.1-μm band depths (Fig. 15). The positions of the Ernutet and Urvara ccps are outside of the general trend in the 2.7- vs 3.4-μm band depths scatterplot, whereas they are consistent with the cluster of ccps in the 3.1 vs 3.4 μm scatterplot.

The 3.4- and 4.0-μm spectral features are both associated with Mg/Ca-carbonates, but the high correlation of the 3.4-μm band (with respect to the 4.0-μm band) with the 3.1-μm absorption band is indicative of the 3.4-μm feature being more related to ammoniated phyllosilicates than the 4.0-μm feature. In fact, the absorption band located at 3.4-μm is not only produced by the overtone of CO_3^{2-}, only, but it is due to contribution of different minerals, especially the NH_4-phyllosilicates (Bishop et al., 2002). The NH_4-annite, for example, shows absorption bands at about 3.1 μm and 3.3 μm (Bishop et al., 2002).

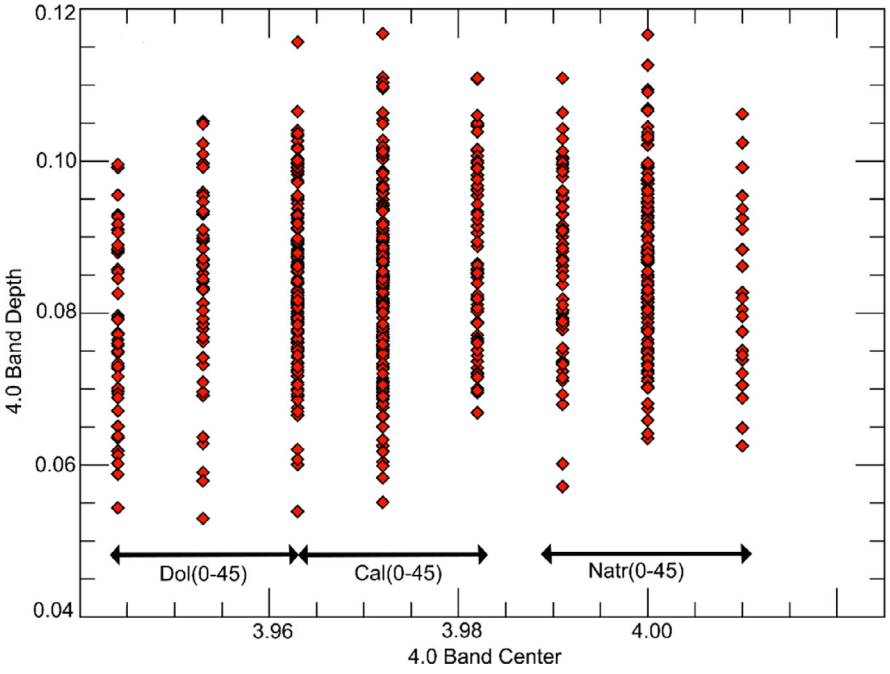

Fig. 8. 4.0-μm band depths vs 4.0-μm band centers for Ikapati ccp (red diamonds), compared to the band centers of dolomite, calcite and natrite, characterized by a grain size of 0–45 μm and sampled to VIR spectral sampling. A large number of Ikapati ccp reflectance spectra are characterized by a band center longward 4.0 μm, suggesting the occurrence of Na-carbonate. (For interpretation of the references to colour in this figure legend, the reader is referred to the web version of this article.)

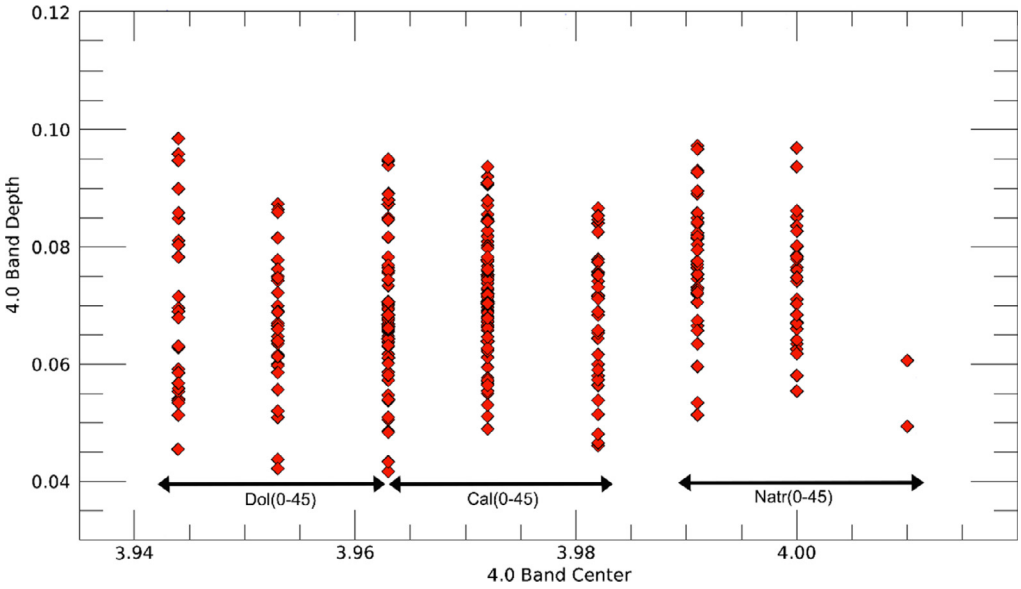

Fig. 9. 4.0-μm band depths vs 4.0-μm band centers for Haulani ccp (red diamonds), compared to the band centers of dolomite, calcite and natrite, characterized by a grain size of 0–45 μm and sampled to VIR spectral sampling. Haulani ccp is also likely composed of a mixture of Mg/Ca-carbonates and Na-carbonates. (For interpretation of the references to colour in this figure legend, the reader is referred to the web version of this article.)

5.4. Variation of spectral parameters with latitude

Starting from the equator and moving toward both north and south poles, a general increase in 2.7-μm band depth is observed (magenta diamonds in Fig. 16). In particular, the P-SD coefficient for the ccps located in the northern hemisphere is (for the ranges described in subchapter 4.4) moderate (0.36 ± 0.02), whereas the P-SD coefficient in the southern hemisphere is stronger (0.68 ± 0.02). These trends are totally different from the general behavior observed on Ceres' surface, represented by the background density plot in Fig. 15, where the highest density (expressed in logarithmic form) is shown by red color and blue color refers to the lowest density. A correlation between band depths and latitude is totally absent in the density plot (the Pearson coefficient is ~ 0 for both hemispheres).

Similarly, band depths of ccps related to NH_4-phyllosilicates (3.1 μm) are deeper at higher latitudes (Fig. 17). Excluding the Dantu ccp from the evaluation of the P-SD coefficient, a general correlation between latitude and 3.1-μm band depths for ccps of the northern hemisphere arises (P-SD is 0.33 ± 0.04). The correlation is stronger (0.71 ± 0.02) for ccps in the southern hemisphere. Band depths of the Cerean surface (background density plot in Fig. 17) do not show a trend with latitude as observed for ccps (the Pearson coefficient is ~ 0 for both the northern and southern hemisphere). Generally, subsurface deposits located at poleward latitudes, and in particular close to the south pole, are probably richer in both Mg-phyllosilicates and NH_4-phyllosilicates than the equatorial subsurface deposits: the OH-group (responsible for the 2.7-μm band) and ammonium-bearing clays (which produce the 3.1-μm band) are probably better preserved at higher latitudes.

Absorption bands related to carbonates do not exhibit a coherent trend at higher latitudes. The 3.4-μm band depth is correlated with latitude in both hemispheres (P-SD values are 0.3 ± 0.005 and

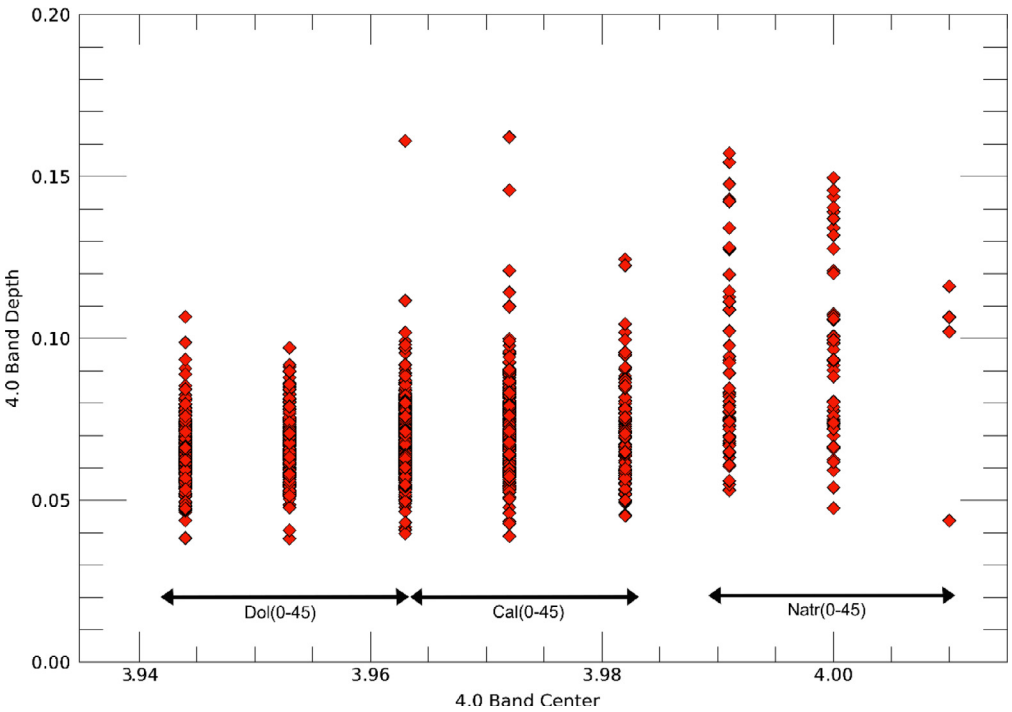

Fig. 10. 4.0-μm band depths vs 4.0-μm band centers for Ernutet ccp (red diamonds), compared to the band centers of dolomite, calcite and natrite, characterized by a grain size of 0–45 μm and sampled to VIR spectral sampling. The mineralogy of the Ernutet ccp is composed of a mixture of Mg/Ca-carbonates and Na-carbonates. (For interpretation of the references to colour in this figure legend, the reader is referred to the web version of this article.)

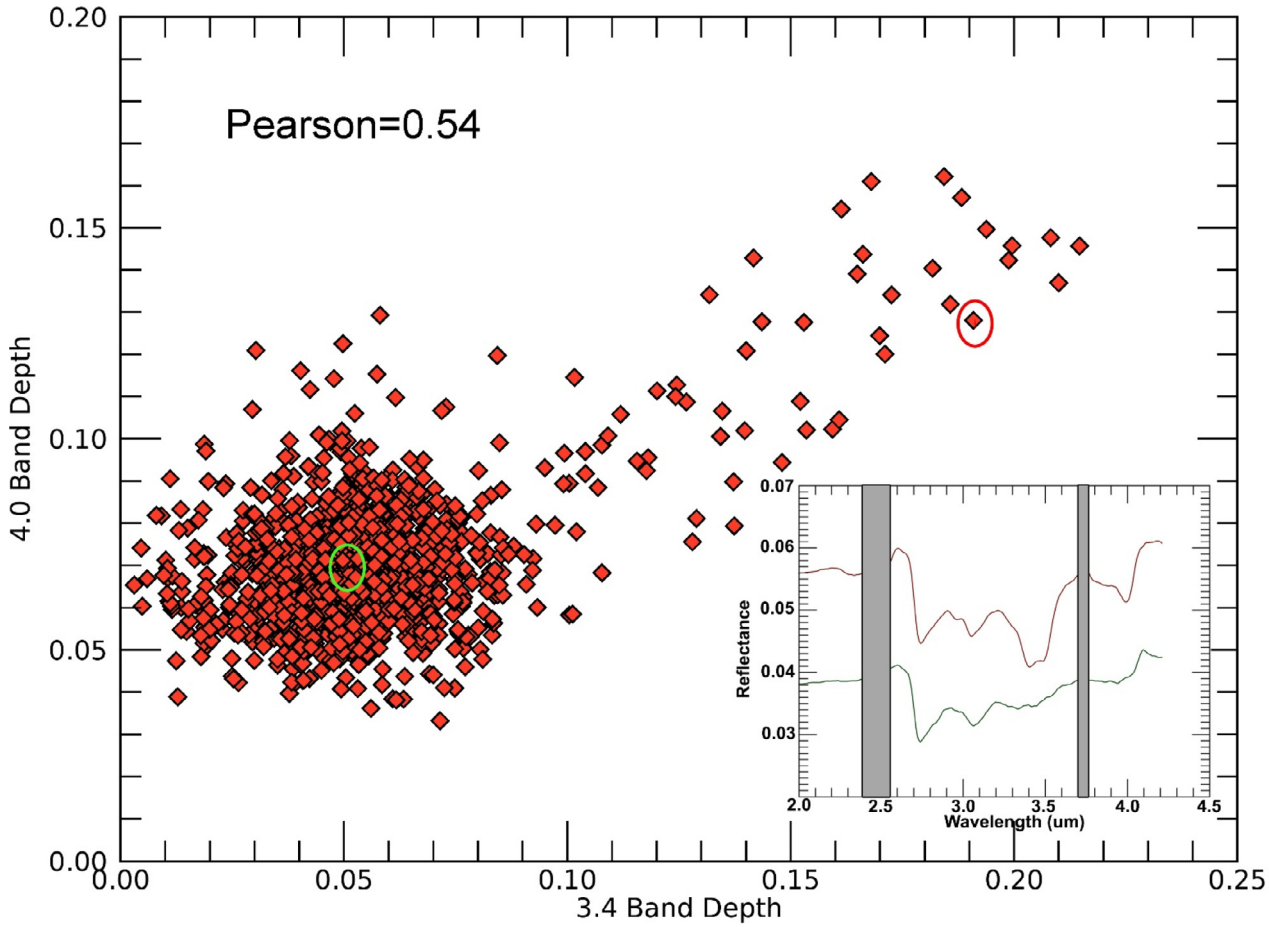

Fig. 11. Scatterplot of 3.4- vs 4.0-μm band depths in the Ernutet ccp (red diamonds). Most of the peak area is composed of calcite and/or dolomite, and the Ernutet representative spectrum is the colored green (belonging to the area of scatterplot included in the green circle). Pixels with strong 3.4- and 4.0-μm bands belong to an area rich in organics (responsible for increasing the 3.4-μm band) and are composed of a mixture of Mg/Ca- and Na-carbonates (for the very strong 4.0-μm band): the representative spectrum of this material is colored red (corresponding to the red diamond marked by red circle). The wavelength ranges affected by spectral artifacts of the VIR filter are shown by the grey bars. (For interpretation of the references to colour in this figure legend, the reader is referred to the web version of this article.)

0.53 ± 0.03 for northern and southern hemispheres, respectively), as can be observed in Fig. 18. The 3.4-μm band depths of Ceres' surface (represented by the density plot on the background of Fig. 18) show a similar but weaker trend with latitude (the Pearson coefficient is 0.2 for the northern hemisphere and 0.45 for the southern one). An opposite behavior is shown by the 4.0-μm band depth of ccps, which can be observed in Fig. 19. In the northern hemisphere, the spatial distribution of carbonate subsurface deposits as a function of 4.0-μm band depth is independent of latitude (the Pearson coefficient is about 0). A weak correlation is obtained in the southern hemisphere (the Pearson value is 0.28). If we exclude peculiar ccps (since they show anomalous values of carbonatic bands in the scatterplot 3.4 vs 4.0 μm band depth of Fig. 7) from the estimation of the coefficient, the absence of a correlation between latitude and 4.0-μm band depths persists in the northern hemisphere, while a Pearson value of 0.67 is obtained for the southern hemisphere, as shown in Fig. 20. This correlation trend is not as robust as in previous cases, since only 6 southern hemisphere ccps are included in the estimation of the Pearson coefficients. An absence of correlation between the 4.0-μm band depths of the entire Ceres surface and latitude (represented by the density plot of Fig. 19) is, instead, observed, both in the northern (Pearson coefficient is 0.1) and southern hemisphere (Pearson coefficient is 0.03). The absence of a particular trend between the 4.0-μm band depth and latitude (both in the subsurface and surface) suggests a global distribution of carbonates on the dwarf planet, probably related to the aqueous alteration experienced by Ceres in the early stage of its formation (Rivkin et al., 2011).

This analysis of ccps highlights, once again, that the 3.4- and 4.0-μm spectral features behave differently, even if they are both associated with carbonates. From the statistical analysis, the 3.4-, the 2.7- and the 3.1-μm band depths increase with latitude, while the 4.0-μm band depth does not show any clear correlation with latitude, although a southern hemisphere anticorrelation is suggested.

Consequently, since the 3.4-μm band assumes, with latitude, a more similar trend with phyllosilicates than with carbonates, the 3.4-μm spectral feature could be the result of a mixed contribution of both carbonates and NH_4-clays.

5.5. Variation of ccps spectral parameters with crater physical parameters

By comparing the 3.4-μm band depth of ccps with their relative crater diameter, we observe a strong correlation (Fig. 21). The P-SD coefficient of 0.65 ± 0.03 is indicative of larger craters having a central uplift where the 3.4-μm spectral feature is deeper. No correlation is observed between diameter and the other studied band depths, i.e., the 2.7-, the 3.1- and the 4.0-μm ones. If the 3.4-μm band is a combination of absorptions due to different minerals (carbonates, NH_4-phyllosilicates and possibly organics), larger craters have central uplifts with

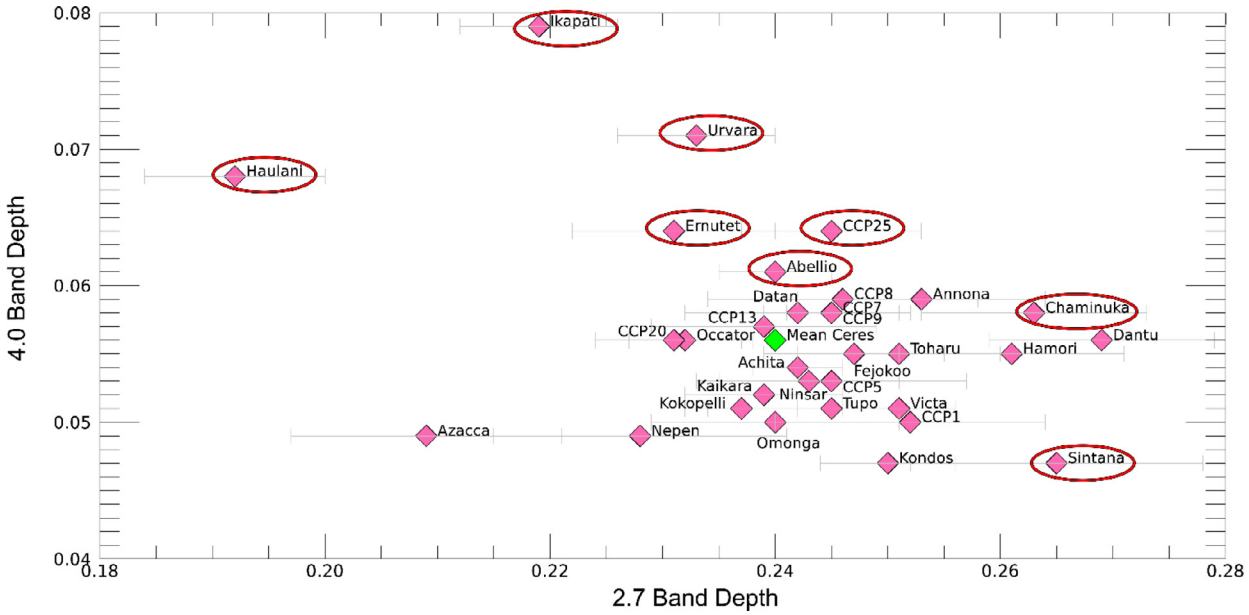

Fig. 12. 2.7- vs 4.0-μm band depths of ccps (grey bar represents standard deviation of 2.7-μm band depth). Excluding Haulani, Ikapati, Urvara, Ernutet, CCP25, Abellio, Chaminuka and Sintana (peculiar ccps, marked by red empty ellipses), Mg/Ca-carbonates appear to be moderately correlated with Mg-phyllosilicates (P-SD coefficient of 0.38 ± 0.002). Green diamond represents the average surface of Ceres. (For interpretation of the references to colour in this figure legend, the reader is referred to the web version of this article.)

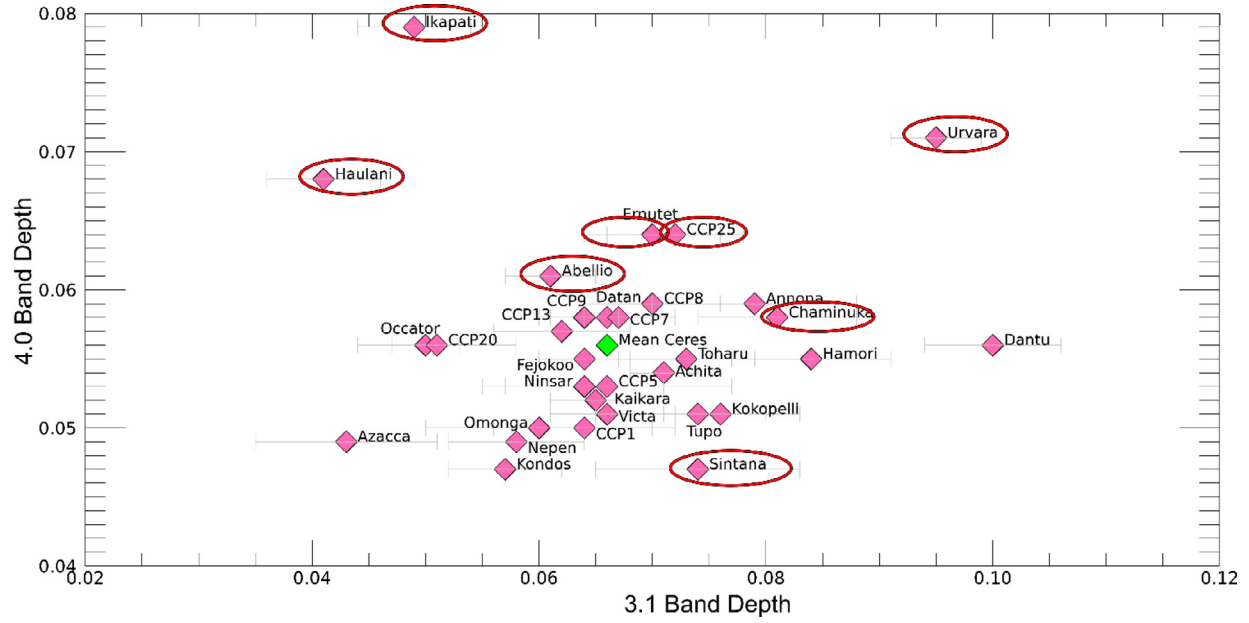

Fig. 13. 3.1- vs 4.0-μm band depths of ccps (grey bar represents standard deviation of 3.1-μm band depth). Excluding Haulani, Ikapati, Urvara, Ernutet, CCP25, Abellio, Chaminuka and Sintana (peculiar ccps, marked by red empty ellipses), Mg/Ca-carbonates are weakly correlated with NH_4-phyllosilicates (P-SD value of 0.3 ± 0.02). Green diamond represents the average surface of Ceres. (For interpretation of the references to colour in this figure legend, the reader is referred to the web version of this article.)

more abundant minerals contributing to the 3.4-μm band. Craters diameters are linearly anticorrelated to the excavation depth, or "pseudo-depth" (Fig. 22), supported by a strong P-SD coefficient of −0.87 ± 0.005, and meaning that larger craters have central peaks that are composed of material coming from deeper within the subsurface. The observed diameter vs 3.4-μm band depth anticorrelation suggests that the mineral mixture responsible for the 3.4-μm absorption is more abundant with increasing depth. Then, by studying ccps where a richer abundance of Na-carbonates has been inferred to occur, i.e., Ernutet, Ikapati and Haulani ccps, we can observe that the resulting pseudo-depth is about 9.00 ± 0.67 km, 8.00 ± 0.58 km and 6.00 ± 0.95 km, respectively.

Band depths of 2.7-, 3.1-, 3.4- and 4.0-μm absorption bands of ccps were compared with the pseudo-depth obtained by the procedure explained in Section 4.3. As expected, the 3.4-μm band depth becomes stronger as the pseudo-depth increases (Fig. 23). The correlation is characterized by a P-SD coefficient of −0.76 ± 0.02. The maximum band depth is obtained in the ccp of Urvara, the largest crater, with a diameter of 170 km. The Urvara ccp is composed of material coming from a depth of about 22 km with respect to the Cerean ellipsoid.

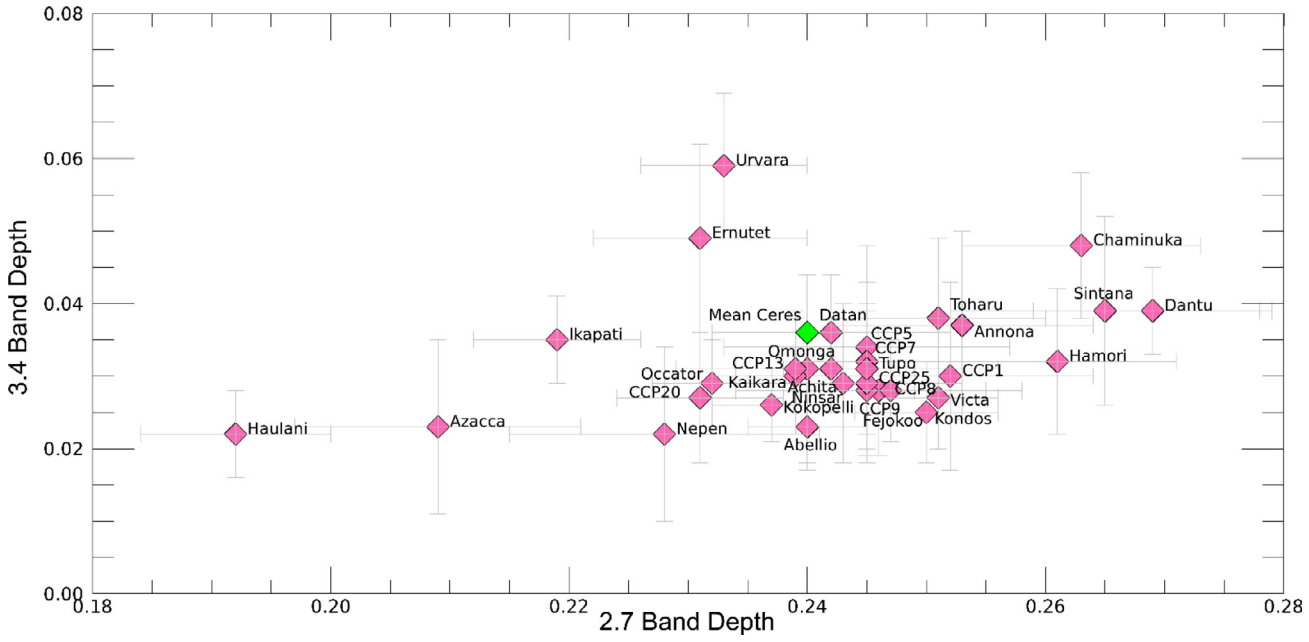

Fig. 14. 2.7- vs 3.4-μm band depths scatterplot of ccps (grey bars represent standard deviations). Excluding Ernutet and Urvara, a moderate correlation is observed, with a P-SD coefficient of 0.4. Green diamond represents the average surface of Ceres. (For interpretation of the references to colour in this figure legend, the reader is referred to the web version of this article.)

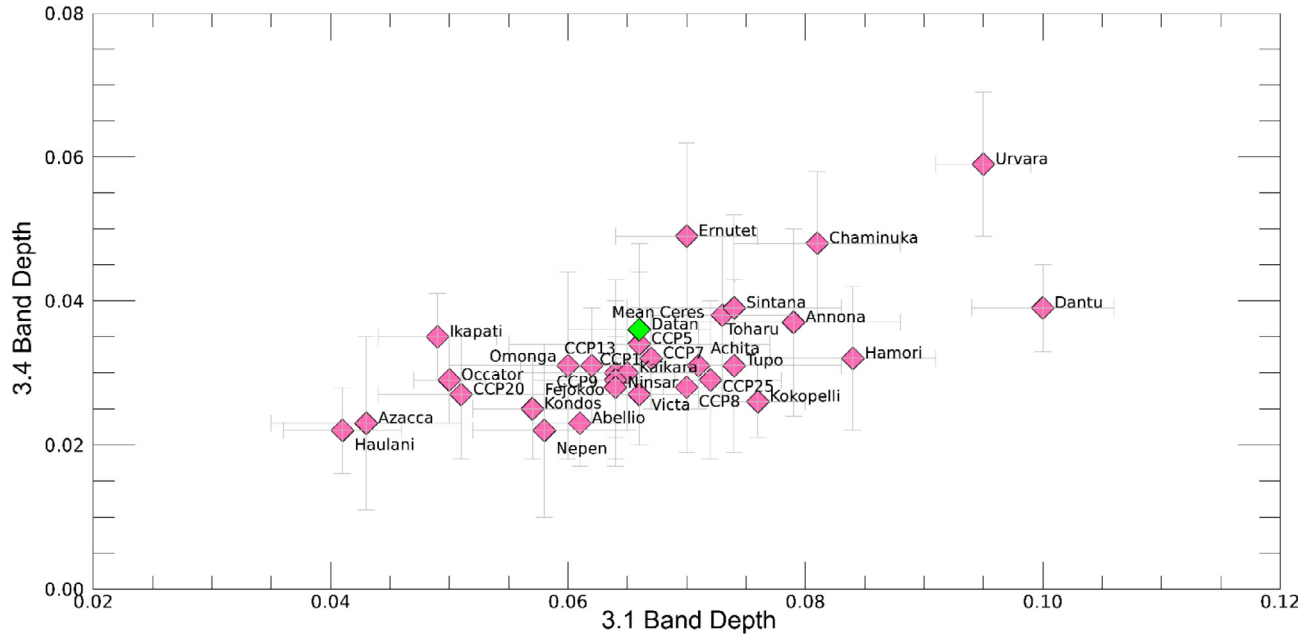

Fig. 15. 3.1- vs 3.4-μm band depths scatterplot of ccps (grey bars represent standard deviations). The P-SD coefficient is 0.58, suggesting a statistically significant correlation between the two spectral parameters. Green diamond represents the average surface of Ceres. (For interpretation of the references to colour in this figure legend, the reader is referred to the web version of this article.)

By comparing the band depth of the 3.1-μm spectral feature with the pseudo-depth (Fig. 24), a similar trend can be observed. Subsurface deposits could be richer in NH_4-phyllosilicates with increasing excavation depth, suggested by a P-SD coefficient of -0.60 ± 0.02. Ccp of Urvara, and Dantu (the central uplifts from the deepest subsurface layers) display the highest values of 3.1-μm band depth; therefore, deposits beneath such craters are likely the richest in NH_4-clays.

A weaker trend is observed by comparing pseudo-depth with both the 2.7-μm band depth (Fig. 25) and the 4.0-μm band depth (Fig. 26). The resulting coefficients are -0.35 ± 0.02 for the 2.7-μm band depth and -0.25 ± 0.005 for the 4.0-μm band depth. By excluding peculiar ccps in the scatterplot of pseudo-depth vs 4.0-μm band depth, the resulting P-SD coefficient has a similar value, i.e., -0.23 ± 0.005. This suggest that carbonates and Mg-phyllosilicates are probably more randomly distributed in the subsurface.

5.6. Possible effects of Ceres space weathering on spectral parameters

Due to its average orbital distance of 2.68 AU from the Sun, the dominant processes involved in the space weathering of Ceres are solar wind irradiation (Gillis-Davis, 2016), micro-meteoritic hypervelocity impacts (Pieters and Noble, 2016) and mixing of materials by impacts.

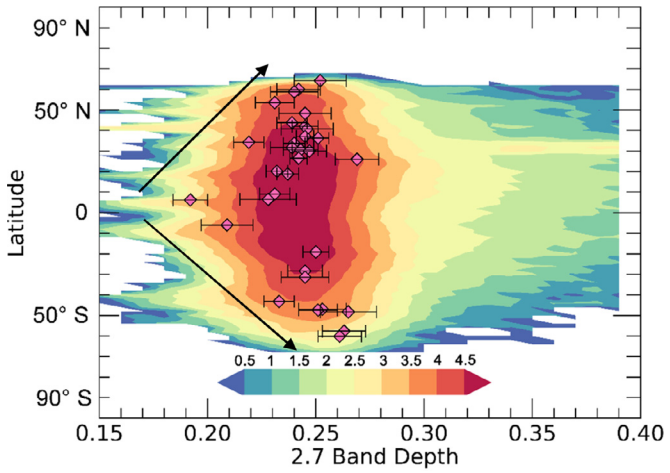

Fig. 16. 2.7-μm band depths of ccps (magenta diamonds) vs latitude (standard deviation of 2.7-μm band depth is shown by dark bar), superimposed on the density plot representing the trend for Ceres surface. Different from the behavior of Ceres surface, band depths of ccps are stronger at higher latitudes. Colorbar refers to the density of pixels forming the density plot, expressed in logarithmic form, where lower values are represented by blue color and higher values by red color. (For interpretation of the references to colour in this figure legend, the reader is referred to the web version of this article.)

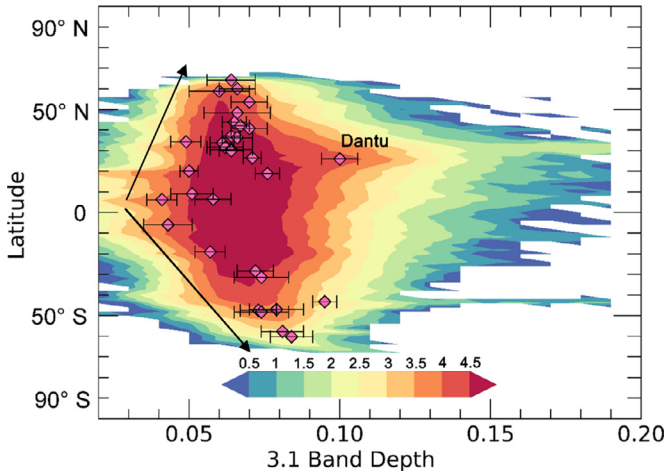

Fig. 17. 3.1-μm band depths of ccps (magenta diamonds) vs latitude (standard deviation of 3.1-μm band depth is shown by dark bar), superimposed on the density plot of Ceres surface. Subsurface deposits located at poleward latitudes are more abundant in NH_4-phyllosilicates. Colorbar refers to the density of pixels in the density plot, expressed in logarithmic form, where lower values are represented by blue color and higher values by red color. (For interpretation of the references to colour in this figure legend, the reader is referred to the web version of this article.)

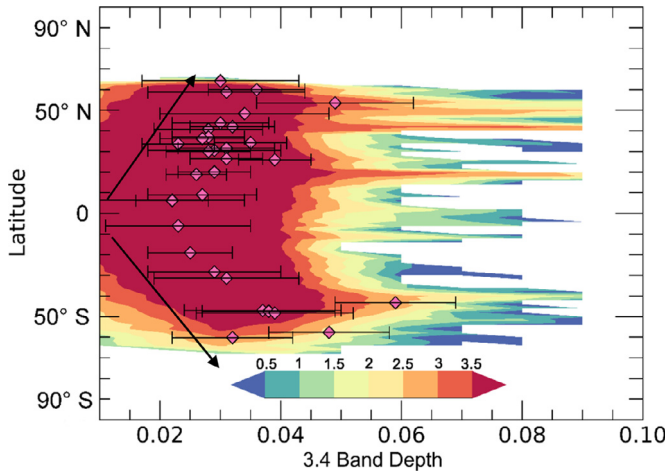

Fig. 18. 3.4-μm band depths of ccps (magenta diamonds) vs latitude (standard deviation of 3.4-μm band depth is shown by dark bar), superimposed on the density plot representing the trend for Ceres' surface. As for 2.7- and 3.1-μm band depths, the P-SD analysis suggests that the 3.4-μm band of ccps is deeper at higher latitude, while a weaker trend is observed for global Ceres surface. Colorbar refers to the density of pixels in the density plot, expressed in logarithmic form, where lower values are represented by blue color and higher values by red color. (For interpretation of the references to colour in this figure legend, the reader is referred to the web version of this article.)

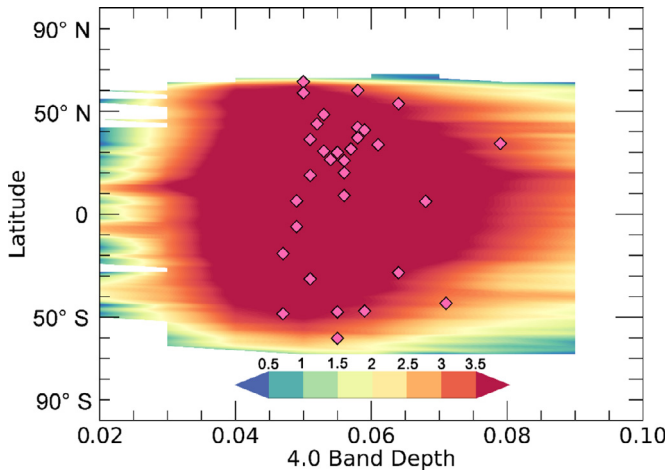

Fig. 19. 4.0-μm band depths of ccps (magenta diamonds) vs latitude, superimposed on the density plot representing the trend for Ceres' surface. No correlation is observed in the northern hemisphere, and a very weak correlation emerges in the southern hemisphere. Colorbar refers to the density of pixels in the density plot, expressed in logarithmic form, where lower values are represented by blue color and higher values by red color. (For interpretation of the references to colour in this figure legend, the reader is referred to the web version of this article.)

Laboratory experiments simulated the effects of solar wind irradiation on primitive asteroids, by performing an ion irradiation on carbonaceous chondrites. The resulting effect in carbonaceous chondrites rich in phyllosilicates is the longward shift of the 2.7-μm absorption band's center due to the loss of magnesium (Lantz et al., 2017). Furthermore, space weathering could also weaken carbonate and phyllosilicate spectral features (Gillis-Davis, 2016).

The 2.7-μm band center was measured for each ccp and related to the formation age of the crater. Similarly, band depths of the 2.7-, 3.1-, 3.4- and 4.0-μm spectral features have been studied as a function of the age of the studied ccps. Neither the shift of the 2.7-μm band center, nor a significant variation in band depths has been noted as a function of the age. A possible explanation is that some minerals appear to be more resistant to space weathering (Gillis-Davis, 2016). Since the band centers and band depths of central uplift's spectral features seem to not to alter with time, they could be representative of the subsurface mineralogy. In addition, crater central uplifts are geologically isolated from the surrounding area, since they are located in the center of crater, and could not be altered and/or mixed with mass moved along the crater walls.

A moderate correlation of spectral slope with the age of ccps is instead noted. The scatterplot in Fig. 27 shows the mean value of the IR slope, estimated between 1.2 and 1.9 μm, as a function of the corresponding age of ccp. The youngest crater, Haulani, is characterized by a bluer (negative) slope, while the rest of the ccps are characterized by redder (positive) slopes, ranging between 0.01 and 0.11. The P-SD coefficient between age and spectral slope is 0.32 ± 0.002. The

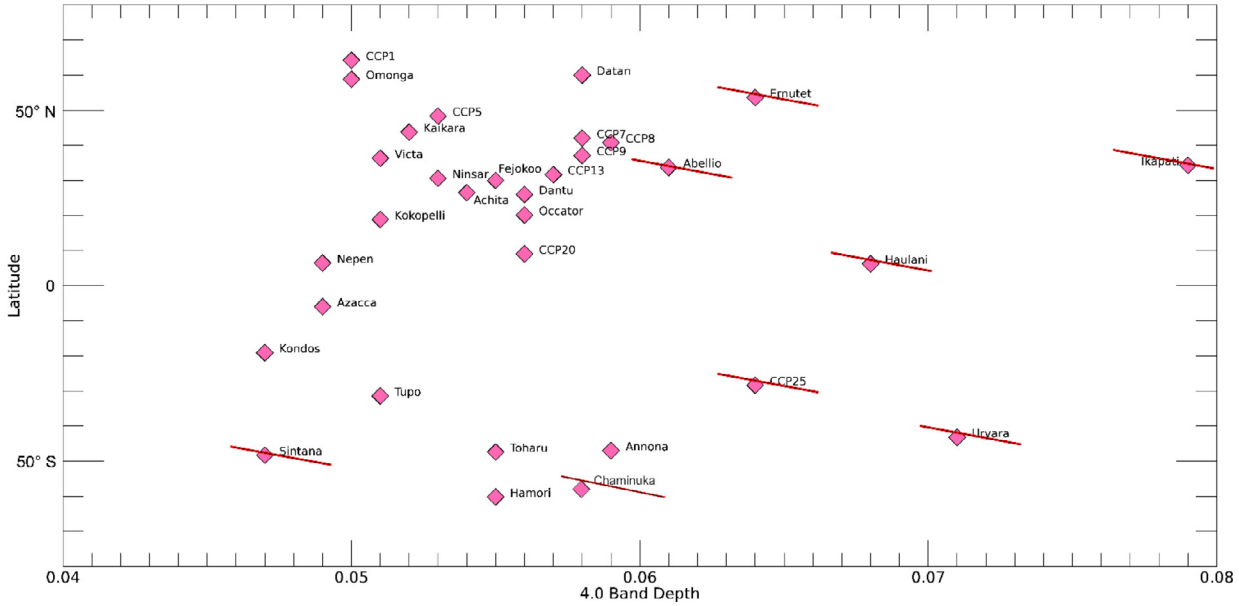

Fig. 20. 4.0-μm band depth vs latitude of ccps (magenta diamonds). The peculiar ccps highlighted by the scatterplot 3.4- vs 4.0-μm band depths (corresponding to Ikapati, Haulani, Abellio, Sintana, Ernutet, Chaminuka, Urvara and CCP25) are, in this case, excluded from the estimation of the Pearson coefficient and the absence of correlation in the northern hemisphere persists. The value in the southern hemisphere is indicative of a strong correlation (0.67). However, for the southern hemisphere, only 6 ccps are included in the Pearson coefficient analysis. (For interpretation of the references to colour in this figure legend, the reader is referred to the web version of this article.)

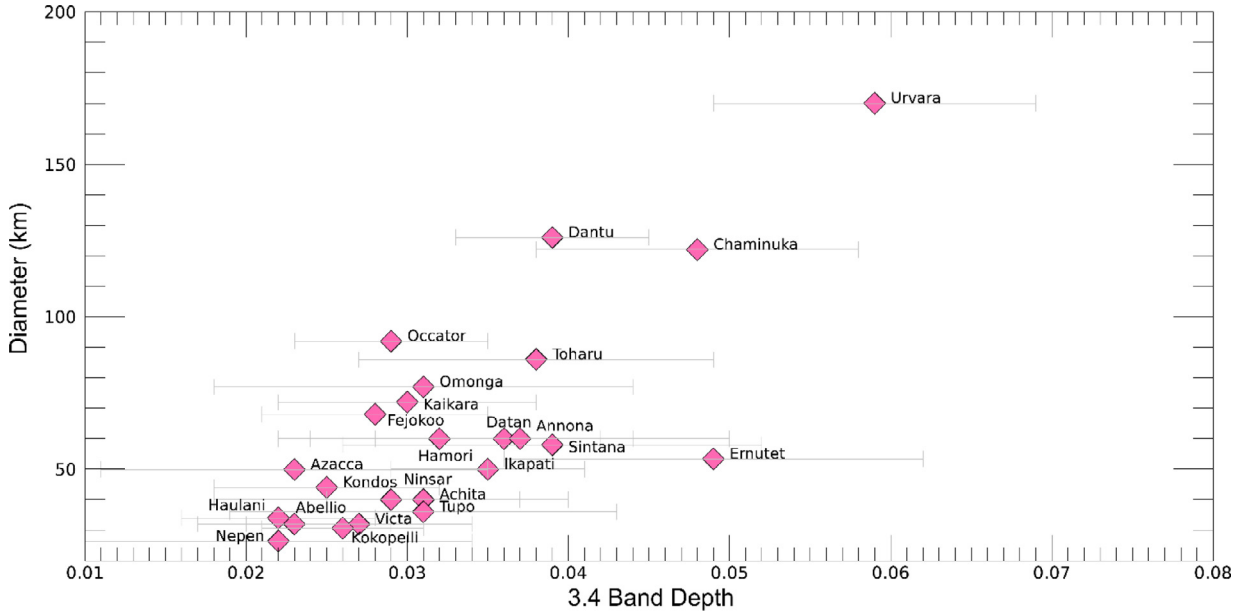

Fig. 21. 3.4-μm band depth of ccps vs diameter of craters containing the relative central peak (standard deviation of 3.4- μm band depth is shown by a grey bar). Spectral features located at 3.4 μm are deeper in the central peaks of larger craters.

variation in spectral slope could be associated with differences in composition or with changes in physical properties (Stephan et al., 2018): laboratory studies demonstrated that the bluer spectral slope is commonly observed in samples with larger grain size (Cloutis et al., 2011). The reddening of the slope in ccps of increasing age could be a clue to the evolution of central uplifts with time: it is likely that the youngest ccps are composed of coarse grained materials that are probably progressively fragmented over time. However, a difference in composition could also produce a bluer slope. For example, while the bluest spectral slope is related to the youngest ccp, i.e., Haulani, Haulani's peak is composed of Na-carbonates mixed with Mg/Ca-carbonates. However, Na-carbonates are also located in the central uplifts of Ernutet and Ikapati ccp, but their slopes are redder and similar to the spectral slope of ccps mainly composed by Mg/Ca-carbonates.

6. Discussion

The analysis of spectral parameters of Ceres ccps, in addition to their latitude and physical parameters (i.e., diameter and depth of excavation), allows us to obtain more information about the possible mineralogy of subsurface deposits. Mg-phyllosilicates and NH_4-phyllosilicates compose the mineralogy of ccps, inferred by the occurrence of absorption bands at 2.7 μm and 3.1 μm, respectively: variations in the strength of such bands are strictly connected, a trend observed also on

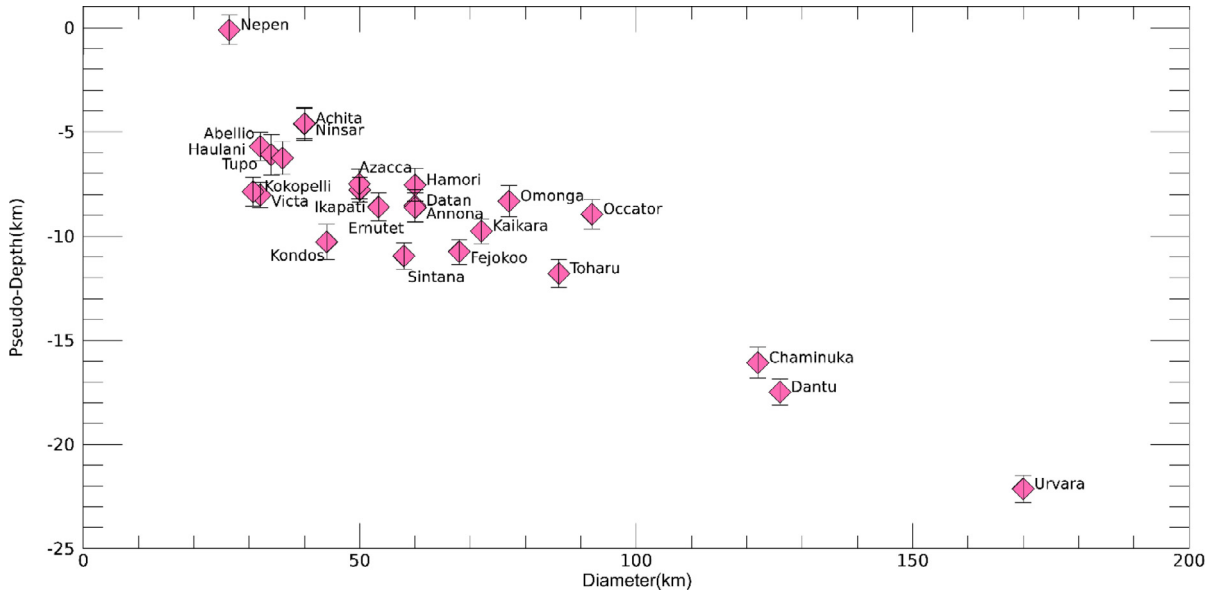

Fig. 22. Depth of excavation of ccps vs crater diameter (standard deviation of pseudo-depth is shown by a grey bar). Larger craters are characterized by ccps coming from greater depths, and ccps rich in Na-carbonates, i.e., Ernutet, Ikapati and Haulani ccps, have arisen, respectively, from about 9, 8 and 6 km within Ceres' surface.

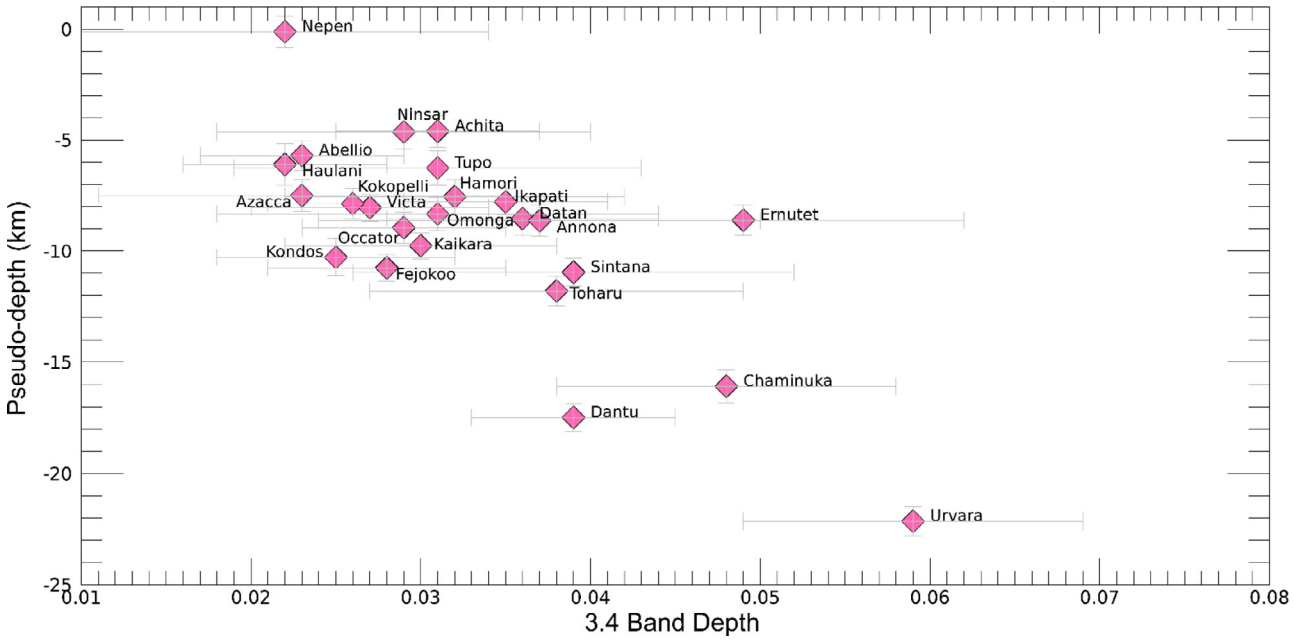

Fig. 23. The 3.4-μm band depth related to the depth of excavation of crater central peak material (standard deviation is shown by a grey bar). The spectral parameter is stronger when material is excavated from a greater depth.

Ceres surface (Ammannito et al., 2016). The abundance of Mg-phyllosilicates and NH_4-phyllosilicates tend to increase in poleward subsurface deposits. This could be indicative of an enrichment of phyllosilicates in the subsurface deposits located at higher latitudes, where the OH-group (responsible for the 2.7-μm band) and ammonium-bearing clays (which produce the 3.1-μm band) are more prominent.

Carbonates are supposed to be responsible for both 3.4- and 4.0-μm bands, a hypothesis supported by their strong correlation, even if some peculiar ccps emerge. Nonetheless, the different behavior of 3.4- and 4.0-μm absorption bands in relation to other parameters suggests a more complex situation. As an example, the correlation between the 3.4-μm band depth and band depth of phyllosilicates' features (i.e., the 2.7 μm and the 3.1 μm band) is stronger than the correlation between the 4.0-μm band depth and band depth of phyllosilicates' features. The strength of the 4.0-μm absorption band seems to not be correlated to latitude. It is reasonable that other components in addition to carbonates could be responsible for the 3.4-μm band strength behavior. The absorption at 3.4 μm could be due to the contribution of different species, such as carbonates, ammoniated phyllosilicates and organics combined in different proportions (Bishop et al., 2002; Nuevo et al., 2014; Moroz et al.,1998). All these species have been detected on Ceres' surface (King et al., 1992; De Sanctis et al., 2015; De Sanctis et al., 2016; De Sanctis et al., 2017; Carrozzo et al., 2018; Longobardo et al., 2018b).

Comparing the band depths of the four absorption bands with the excavation depth from which ccps originate, it emerges that the 3.1- and 3.4-μm bands are stronger with increasing excavation depth, while a weak correlation is observed for the 2.7- and 4.0-μm band depths with excavation depth. Phyllosilicates and carbonates are likely the product of interactions, at low temperature, between rock and aqueous fluid

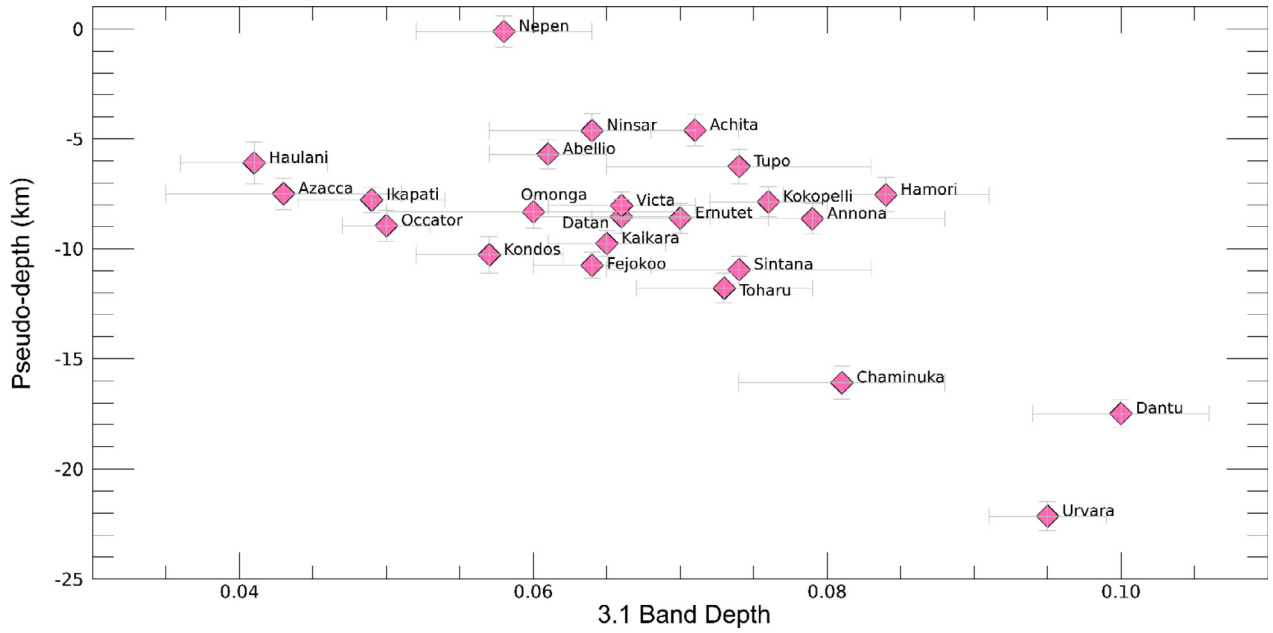

Fig. 24. 3.1-μm band depth vs crater depth (standard deviation is shown by a grey bar). Ammoniated phyllosilicates are more abundant in deeper subsurface deposits, located beneath Urvara and Dantu craters.

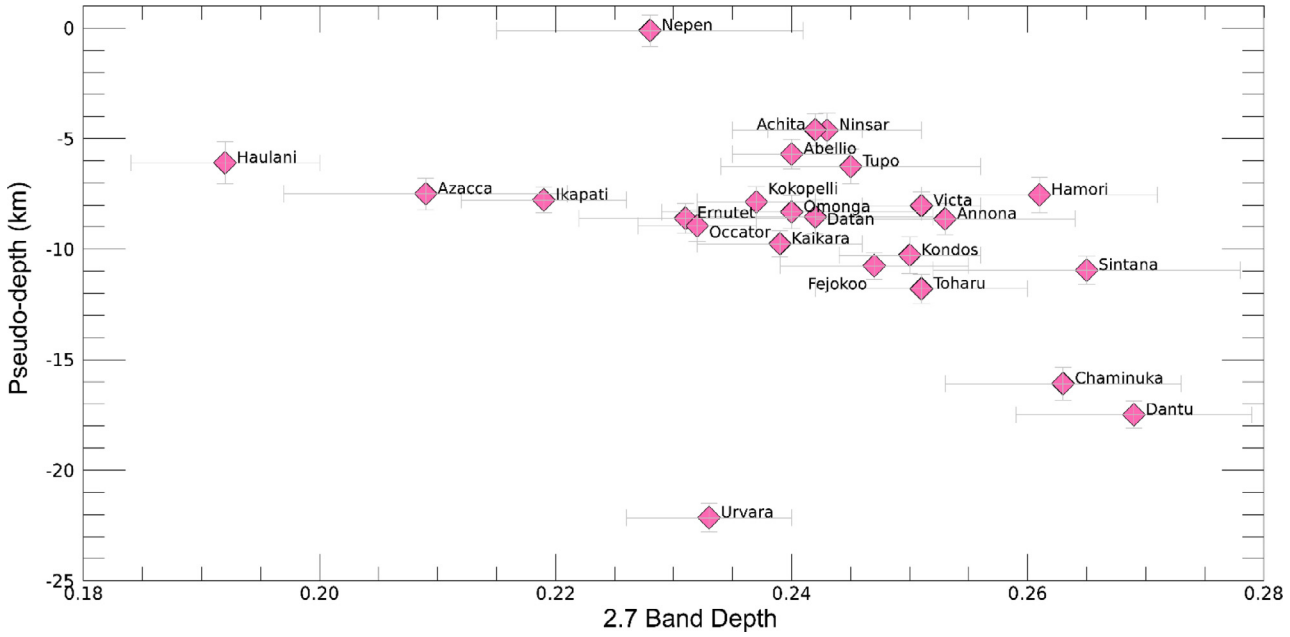

Fig. 25. Scatterplot of 2.7-μm band depth vs pseudo-depth (standard deviation is shown by a grey bar), where a moderate anti-correlation is observed.

(Neveu et al., 2017): basing on the models proposed to describe the Ceres interior (Castillo-Rogez, 2011; Travis and Feldman, 2016; Ermakov et al., 2017; Fu et al., 2017) and the increasing strength of absorption bands (in particular of ammoniated phyllosilicates) with depth of excavation, we suppose that our investigation reached subsurface layers nearby the boundary between volatile-rich crust and silicate-rich mantle (Ermakov et al., 2017).

Considering that the 3.4-μm band is both linked to the 4.0 μm one, and to the 2.7- and 3.1-μm bands, this spectral feature could be the result of the contribution of both carbonates and ammonium-phyllosilicates. Only in specific places, such as Ernutet crater, can this absorption be influenced by the presence of organics. Furthermore, both the 3.1-μm and the 3.4-μm band depths strongly increase with excavation depth, indicating that the 3.4-μm spectral feature is mainly the result of absorptions due to both carbonates and NH_4-phyllosilicates. In fact, ammoniated phyllosilicates such as the NH_4-annite have absorption bands at about 3.1 μm and 3.3 μm (Bishop et al., 2002), and the latter could contribute to the strength and shape of the 3.4-μm absorption band in reflectance spectra of the ccps.

The 4.0-μm absorption band is generally attributed to Mg/Ca-carbonates, as well as calcite, dolomite, magnesite and Na-carbonates, such as natrite (De Sanctis et al, 2015; De Sanctis et al., 2016). In particular, when observed, the large band depths, in addition to the shift of band centers towards 4.0 μm, are indicative of the occurrence of Na-carbonates. These minerals are suggested to be located within the Ernutet, Haulani and Ikapati ccps and the excavation pseudo-depth of these central peaks ranges from ~ 6 to ~ 9 km. The association of Na-carbonate with young craters could be consistent with material uplifted

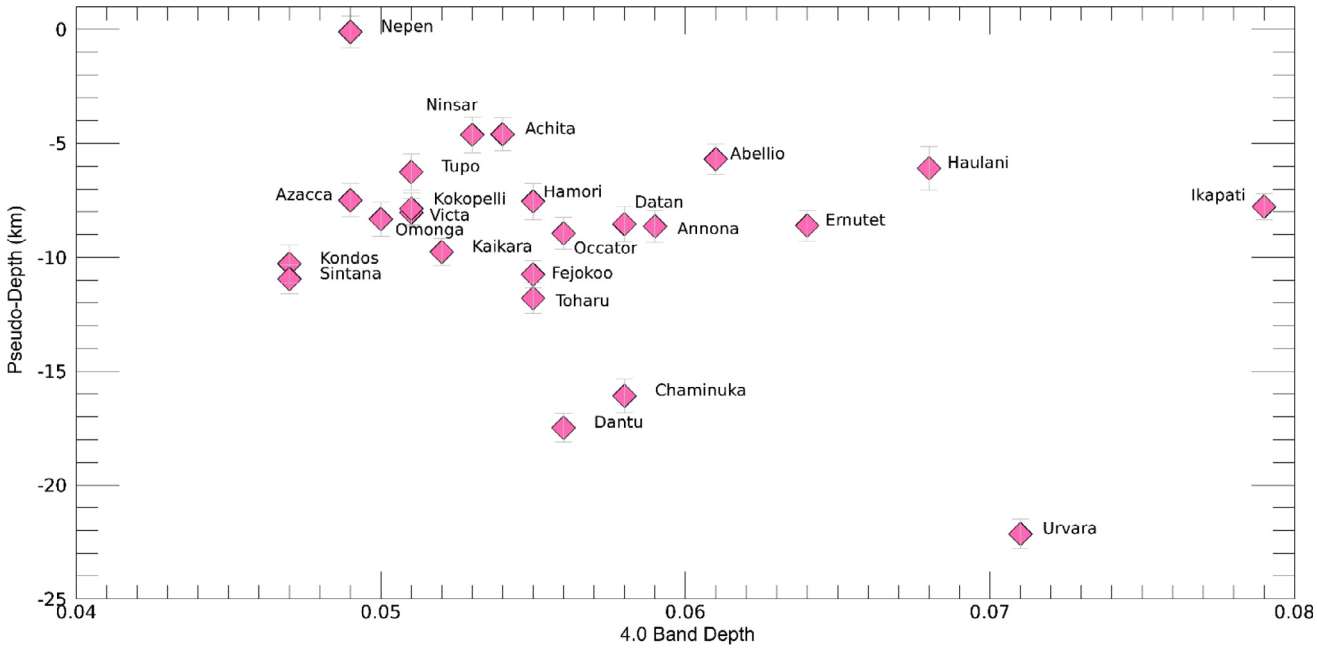

Fig. 26. Scatterplot of 4.0-μm band depth vs pseudo-depth (standard deviation is shown by a grey bar), where a very weak anti-correlation emerges.

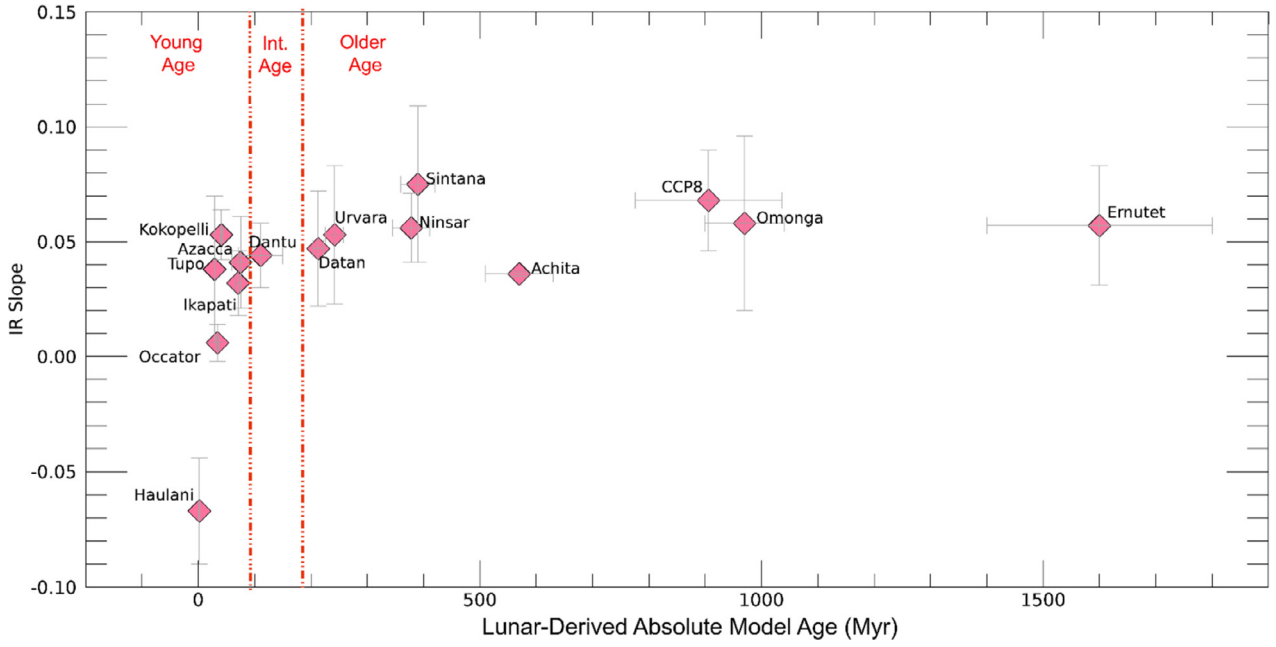

Fig. 27. Scatterplot of age vs IR slope of ccps. For each value, the standard deviation is shown by a grey bar. Ccps with formation ages less than 80 Myr are part of the "Young Age"; the "Intermediate Age" involves ccps with ages between 80 and 180 Myr; and the oldest ccps, with ages greater than 180 Myr are part of "Older Age". A moderate correlation is observed, with a P-SD coefficient of 0.32 ± 0.002.

or created by impact-induced heating (Carrozzo et al., 2018). In the first hypothesis, it likely that reservoirs of Na-carbonates could lie at depth and be extruded onto the surface through cryovolcanic processes (Carrozzo et al., 2018). The impact-induced heating could, instead, melt ice and produce aqueous solutions containing ions as Na^+ and CO_3^{2-}, NH_4^+ and HCO_3^-. The freezing and evaporation allows the precipitation of corresponding salts. Na-carbonates of various hydration states are the first and most abundant precipitates (Vu et al., 2017; Zolotov, 2017). Deposits of Na-carbonates could be present in the subsurface and, regardless of their formation process, the Na-carbonate emerges to the surface when the central peak forms.

Na-carbonates in Occator ccp are absent or very reduced, different from the bright spots located on the dome (Cerealia Facula) and floor (Vinalia Faculae). Cerealia Facula is younger than the crater itself, formed about 30 Myr later (Nathues et al., 2017): perhaps the event that produced Occator crater released sufficient energy to activate processes that eventually produced the central bright spot by ascension of bright material, including Na-carbonates, from a subsurface reservoir (Nathues et al., 2017).

Ccps appear to be minimally altered by space weathering, which includes processes such as solar wind irradiation, micro-meteoritic hypervelocity impacts and mixing of materials by impacts: neither shifts in the band centers nor variations in the strength of absorption bands emerge with increasing age. Consequently, band center positions

Table 2
Summary of the abundance of each mineral (Mg-phyllosilicates, NH_4-phyllosilicates and carbonates) in both peculiar ccps and cluster of ccps with respect to the average Ceres. The depletion of minerals with respect to the Ceres average is expressed as "Low abundance", an abundance similar to that of mean Ceres is termed as "Average abundance", the enrichment is indicated with "High abundance" and a moderate abundance, intermediate between Ceres average and the "High abundance" is expressed as "Average-to-high abundance".

	Mg-phyllosilicates	NH_4-phyllosilicates	Carbonates
Cluster of ccps	Average abundance	Average abundance	Average abundance
Ikapati	Low abundance	Low abundance	High abundance
Haulani	Low abundance	Low abundance	High abundance
Ernutet	Average abundance	Average abundance	High abundance
CCP25	Average abundance	Average abundance	Average-to-high abundance
Abellio	Average abundance	Average abundance	Average-to-high abundance
Urvara	Average abundance	High abundance	High abundance
Sintana	High abundance	Average abundance	Low abundance
Chaminuka	High abundance	High abundance	Average abundance

and values of band depths of ccps are likely representative of the subsurface deposits from where they originated. The effects of space weathering probably emerge in the spectral slope. The bluer spectral slope in younger ccps could suggest that, when the uplift occurs, it is composed of coarse grains, whose average size declines with time, producing a redder spectral slope – a process seen in carbonaceous chondrite reflectance spectra (Johnson and Fanale, 1973). Also, a different mineral composition could produce a bluer slope: the occurrence of Na-carbonates could be responsible of the negative slope observed in Haulani. However, Na-carbonates are also within the Ikapati and Ernutet ccps, which are not characterized by negative slopes. The fragmentation of regolithic material composing the central uplifts with time is, probably, the most plausible explanation for the trend observed between age and spectral slope.

6.1. Investigation of peculiar ccps

In the scatterplot of 3.4 vs 4.0 μm band depth (Fig. 7), some peculiar ccps emerged, since their position was outside of the main cluster of ccps. Taking into account the results obtained from the analysis performed, we propose explanations for the different behavior of peculiar ccps. First, we reiterate that the 4.0-μm spectral feature is due to both Mg/Ca-carbonates and Na-carbonates (Carrozzo et al., 2018), and the position of this band can be used to constrain possible carbonates. The 3.4-μm absorption band is probably the result of contributions from both carbonates and NH_4-phylloslilicates (that are also responsible for the 3.1-μm spectral feature). In the case of the Ernutet ccp, organics also contribute to the absorption at 3.4 μm.

Generally, each ccp is composed of carbonates, Mg-phyllosilicates and NH_4-phyllosilicates, in addition to the dark component common to the entire surface of Ceres, but their relative abundances can vary, producing peculiar ccps. Observing Fig. 7, we suggest that the cluster of ccps with a 4.0-μm band depth lower than 0.06 are mainly composed of Mg/Ca-carbonates. For 4.0-μm band depth values between 0.06 and about 0.073, an intermediate region can be marked, where Mg/Ca-

Extended data 1
In the following table, parameters used to perform spectral analysis of ccps are listed. Columns describe: names of studied ccps; 2.7-μm band depths (2.7BD) and their standard deviation (SD); 3.1-μm band depths (3.1BD) and relative SD; 3.4-μm band depths and SD; spectral slope estimated between 1.2 and 1.9 μm (SLOPE) and relative SD; 4.0-μm band centers (4.0BC); 4.0-μm band depths (4.0BD); Pseudo-depth (P.-D.) and relative error. Standard deviations and errors reported here are those used in the estimation of the P-SD coefficient. The 4.0-μm band centers and the 4.0-μm band depths are estimated directly from mean spectra of ccps, therefore they lack standard deviation.

Name	2.7BD	SD	3.1BD	SD	3.4BD	SD	SLOPE	SD	4.0BC	4.0BD	P.-D. (km)	Error (km)
CCP1	0.252	0.012	0.064	0.008	0.030	0.013	0.060	0.037	3.953	0.05	–	–
Datan	0.242	0.01	0.066	0.006	0.036	0.008	0.047	0.025	3.944	0.058	−8.54	0.77
Omonga	0.240	0.011	0.060	0.01	0.031	0.013	0.058	0.038	3.944	0.05	−8.32	0.75
Ernutet	0.231	0.009	0.07	0.006	0.049	0.013	0.057	0.026	3.963	0.064	−8.60	0.67
CCP5	0.245	0.012	0.066	0.011	0.034	0.014	0.064	0.034	3.953	0.053	–	–
Kaikara	0.239	0.007	0.065	0.004	0.03	0.008	0.06	0.017	3.953	0.052	−9.76	0.59
CCP7	0.245	0.006	0.067	0.003	0.032	0.007	0.072	0.014	3.953	0.058	–	–
CCP8	0.246	0.012	0.07	0.006	0.028	0.009	0.068	0.022	3.953	0.059	–	–
CCP9	0.245	0.004	0.064	0.003	0.028	0.006	0.068	0.018	3.953	0.058	–	–
Victa	0.251	0.005	0.066	0.005	0.027	0.007	0.062	0.023	3.944	0.051	−8.04	0.61
Ikapati	0.219	0.007	0.049	0.005	0.035	0.006	0.032	0.014	3.963	0.079	−7.78	0.58
Abellio	0.240	0.005	0.061	0.004	0.023	0.006	0.06	0.014	3.963	0.061	−5.7	0.68
CCP13	0.239	0.01	0.062	0.006	0.031	0.008	0.062	0.012	3.953	0.057	–	–
Ninsar	0.243	0.008	0.064	0.007	0.029	0.011	0.056	0.015	3.944	0.053	−4.63	0.79
Fejokoo	0.247	0.008	0.064	0.004	0.028	0.007	0.065	0.009	3.953	0.055	−10.75	0.6
Achita	0.242	0.004	0.071	0.003	0.031	0.006	0.036	0.001	3.953	0.054	−4.6	0.72
Dantu	0.269	0.01	0.1	0.006	0.039	0.006	0.044	0.014	3.953	0.056	−17.49	0.62
Occator	0.232	0.005	0.05	0.003	0.029	0.006	0.006	0.008	3.934	0.056	−8.95	0.7
Kokopelli	0.237	0.005	0.076	0.004	0.026	0.005	0.053	0.011	3.953	0.051	−7.86	0.69
CCP20	0.231	0.007	0.051	0.007	0.027	0.009	0.012	0.013	3.963	0.056	–	–
Nepen	0.228	0.013	0.058	0.006	0.022	0.012	0.054	0.029	3.953	0.049	−0.11	0.71
Haulani	0.192	0.008	0.041	0.005	0.022	0.006	−0.067	0.023	3.972	0.068	−6.1	0.95
Azacca	0.209	0.012	0.043	0.008	0.023	0.012	0.041	0.020	3.953	0.049	−7.5	0.72
Kondos	0.25	0.006	0.057	0.005	0.025	0.007	0.058	0.013	3.953	0.047	−10.28	0.83
CCP25	0.245	0.008	0.072	0.006	0.029	0.011	0.054	0.022	3.953	0.064	–	–
Tupo	0.245	0.011	0.074	0.009	0.031	0.012	0.038	0.032	3.944	0.051	−6.26	0.79
Urvara	0.233	0.007	0.095	0.004	0.059	0.01	0.053	0.03	3.944	0.071	−22.15	0.66
Annona	0.253	0.011	0.079	0.009	0.037	0.013	0.060	0.042	3.963	0.059	−8.64	0.7
Toharu	0.251	0.009	0.073	0.006	0.038	0.011	0.069	0.012	3.953	0.055	−11.79	0.67
Sintana	0.265	0.013	0.074	0.009	0.039	0.013	0.075	0.070	3.953	0.047	−10.95	0.63
Chaminuka	0.263	0.01	0.081	0.007	0.048	0.01	0.037	0.073	3.953	0.058	−16.08	0.74
Hamori	0.261	0.01	0.084	0.007	0.032	0.01	0.073	0.054	3.953	0.055	−7.55	0.79

Extended data 2
the columns list the names of ccps, their crater diameter, the expression lr_p-e_p, the pseudo-depth (p.-d.) and its error $\sigma_{p.-d.}$.

Name	Diameter (km)	lr_p-e_p (km)	p.-d. (km)	$\sigma_{p.-d.}$ (km)
CCP1	–	−0.684	–	–
Datan	60	−2.563	−8.54	0.77
Omonga	77	−0.623	−8.32	0.75
Ernutet	53,4	−3.264	−8.60	0.67
CCP5	–	−1.33	–	–
Kaikara	72	−2.56	−9.76	0.59
CCP7	–	−2.605	–	–
CCP8	–	0.375	–	–
CCP9	–	1.416	–	–
Victa	32	−4.835	−8.04	0.61
Ikapati	50	−2.778	−7.78	0.58
Abellio	32	−2.497	−5.7	0.68
CCP13	–	1.304	–	–
Ninsar	40	−0.628	−4.63	0.79
Fejokoo	68	−3.953	−10.75	0.6
Achita	40	−0.601	−4.6	0.72
Dantu	126	−4.887	−17.49	0.62
Occator	92	0.253	−8.95	0.7
Kokopelli	30.7	−4.792	−7.86	0.69
CCP20	–	−1.311	–	–
Nepen	26,4	2.528	−0.11	0.71
Haulani	34	−2.695	−6.1	0.95
Azacca	49,91	−2.506	−7.5	0.72
Kondos	44	−5.877	−10.28	0.83
CCP25	–	−2.086	–	–
Tupo	36	−2.656	−6.26	0.79
Urvara	170	−5.147	−22.15	0.66
Annona	60	−2.635	−8.64	0.7
Toharu	86	−3.192	−11.79	0.67
Sintana	58	−5.152	−10.95	0.63
Chaminuka	122	−3.884	−16.08	0.74
Hamori	60	−1.546	−7.55	0.79

carbonates and Na-carbonates may compose ccps as a mixture. For higher values of 4.0 μm band depths, ccps are mainly composed of Na-carbonates, mixed with Mg/Ca-carbonates. Also taking into account the scatterplot of 2.7 vs 3.1-μm band depth in Fig. 5 we can analyze the abundance of NH_4-phyllosilicates in the ccps and estimate their contribution to the 3.4-μm absorption band.

Ikapati ccp is composed of Na-carbonates mixed with Mg/Ca-carbonates, characterized by a high value of 4.0-μm band depth. Mg-phyllosilicates and NH_4-phyllosilicates are reduced in Ikapati's ccp. Therefore, the contribution of ammoniated phyllosilicates in the 3.4-μm absorption band is minimal, and carbonates should be the main contributor to this spectral feature.

Similarly, the Haulani ccp is depleted in Mg- and NH_4-phyllosilicates, and it is composed of a high abundance of Mg/Ca- and Na-carbonates. The 3.4-μm spectral feature could be, therefore, mainly produced by carbonates.

The Ernutet ccp is rich in both Mg/Ca-carbonates and Na-carbonates. Organics also compose the Ernutet ccp, as evidenced by a strong increase of the 3.4-μm band and by the peculiar shape of the absorption (De Sanctis et al., 2017) in some reflectance spectra of the peak area. Observing the position of the Ernutet ccp in the phyllosilicates scatterplot of Fig. 5, we can observe that the abundance of phyllosilicates is similar to that of Ceres' average. Therefore, in the case of the Ernutet ccp, the mean value of the 3.4-μm band depth is probably attributable to carbonates, organics and NH_4-phyllosilicates.

The CCP25 and Abellio ccp also show values of 2.7- and 3.1-μm band depths included in the cluster of ccp. However, the 4.0-μm band depths are higher than the values of the ccp cluster but are lower than the values of the Haulani and Ikapati ccps. Consequently, the 3.4-μm spectral feature of these ccps could be the result of both carbonates and NH_4-phyllosilicates. The CCP25 and Abellio ccp are the closest to the cluster of ccps in the scatterplot of 3.4 vs 4.0 μm band depth, therefore their composition could be similar to most ccps in terms of minerals associated with these absorption features.

Urvara ccp is very peculiar, since it is very rich in ammoniated clays, whereas the Mg-phyllosilicates abundance is similar to the cluster of ccps. Regardless, it is composed of a large amount of Mg/Ca-carbonates. Both ammoniated minerals and carbonates could strongly contribute to the 3.4-μm spectral feature.

Sintana ccp is depleted in Mg/Ca-carbonates and rich in Mg-phyllosilicates. The abundance of NH_4-phyllosilicates is similar to the Cerean average. Consequently, the 3.4-μm absorption band could be mainly due to the contribution of ammoniated minerals.

The Chaminuka ccp shows a high abundance of both Mg-phyllosilicates and NH_4-phyllosilicates, whereas carbonatic material occurs in abundance similar to the cluster. Ammoniated phyllosilicates, therefore, could contribute to the shape and strength of 3.4-μm absorption band with more relevance than carbonates.

The differences between peculiar ccps, cluster of ccps and Ceres average, relative to the abundance of carbonates, Mg-phyllosilicates and NH_4-phyllosilicates, are summarized in Table 2.

The different contribution of carbonates and NH_4-phyllosilicates in the Cerean ccps is reflected in the shape of the 3.4-μm absorption band, as observed in Fig. 28, where the mean reflectance spectra of peculiar ccps are shown. Furthermore, the isolated 3.4-μm spectral feature of ccps, i.e., obtained after the continuum removal and normalization to 3.68 μm, can be observed in Fig. 29. In the spectrum of the Chaminuka ccp (dark green spectrum), the 3.4-μm absorption band, which is probably mainly related to ammoniated clays, is characterized by a

Extended data 3
In the following table, the statistical coefficients are summarized. In particular, the P-SD coefficients are reported with their standard deviation. Data between brackets refer to P-SD values where peculiar ccps are excluded.

	2.7BD	3.1BD	3.4BD	4.0BD	AGE (LDM)	P.-D.
2.7BD	–	0.66 ± 0.02	0.41 ± 0.04	−0.33 ± 0.02 (0.38 ± 0.02)	–	–
3.1BD	–	–	0.63 ± 0.03	0.06 ± 0.02 (0.3 ± 0.02)	–	–
3.4BD	–	–	–	0.47 ± 0.03 (0.58 ± 0.05)	–	–
Slope	–	–	–	–	0.32 ± 0.002	
Latitude	0.36 ± 0.002 (North Emi.) 0.68 ± 0.02 (South Emi.)	0.33 ± 0.04 (North Emi.) 0.71 ± 0.02 (South Emi.)	0.3 ± 0.05 (North Emi.) 0.53 ± 0.03 (South Emi.)	No correlation (North Emi.) 0.28 (South Emi.) (0.67) (South Emi.)	–	–
P.-D.	−0.35 ± 0.02	−0.60 ± 0.02	−0.76 ± 0.02	−0.25 ± 0.005 (−0.23 ± 0.005)	–	–
Diameter	–	–	0.65 ± 0.03	–	–	−0.87 ± 0.005

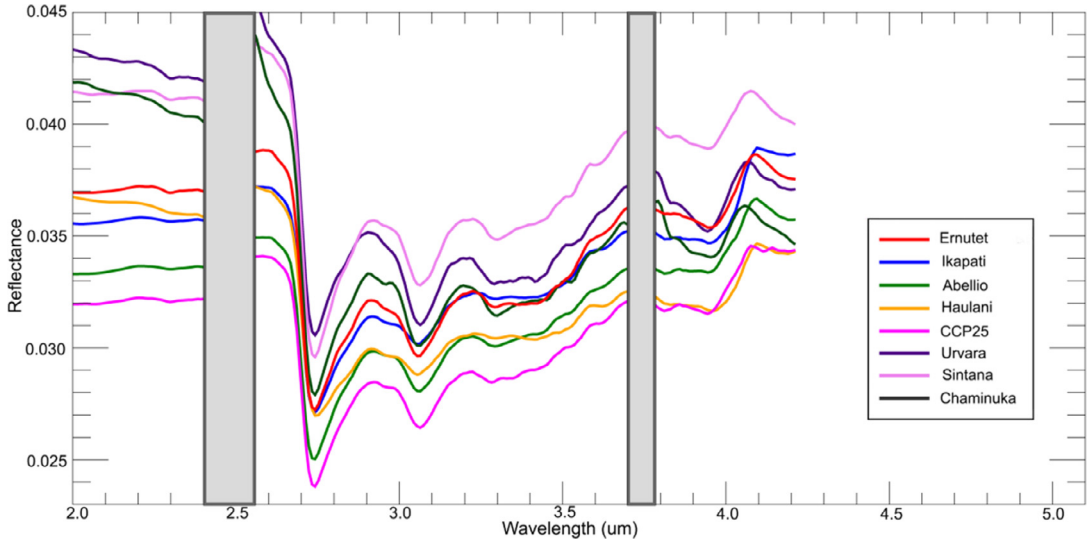

Fig. 28. Mean reflectance spectra of peculiar ccps. The different contribution of NH_4-phyllosilicates, carbonates and organics produce a different shape of the 3.4-μm spectral feature. The grey areas mark the wavelength intervals where the contribution of VIR filters covers the signal from Ceres.

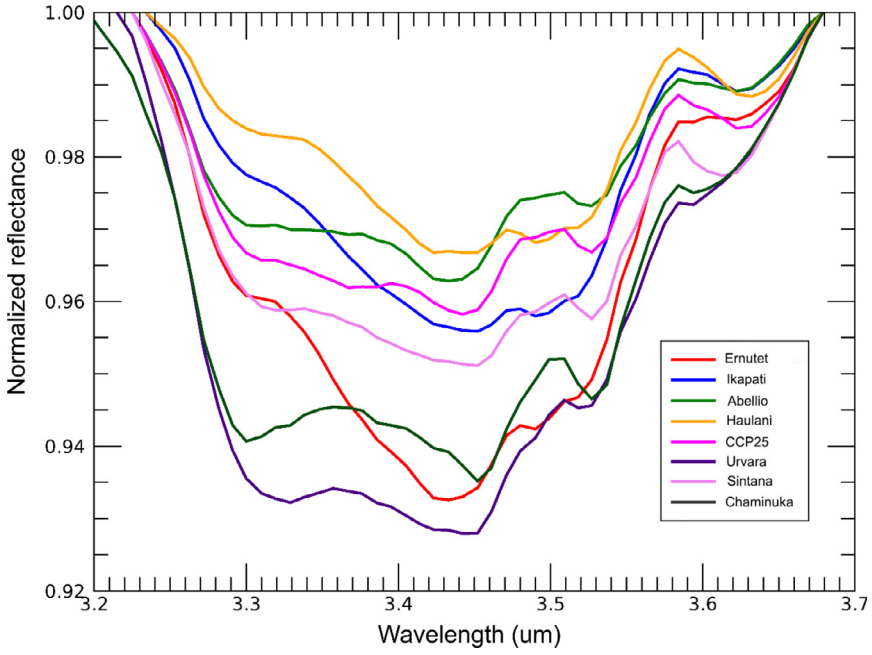

Fig. 29. 3.4-μm absorption bands of peculiar ccps normalized at 3.68 μm, obtained after the removal of spectral continuum in mean reflectance spectra.

deep absorption at about 3.3 μm, very similar to that observed in the reflectance spectrum of NH_4-annite (Bishop et al., 2002). The 3.4-μm absorption band of the CCP25 (magenta spectrum) and Abellio ccps (green spectrum), probably due to both ammoniated minerals and carbonates, assume a different shape: the 3.3-μm feature is not evident as in the Chaminuka ccp, and the band has a more "round" shape. The 3.4-μm band in the mean spectrum of the Urvara ccp (violet spectrum) is characterized by a minimum at about 3.45 μm, probably due to residual artifacts in the VIR spectra, hiding the absorption at 3.3 μm that should be evident for the high abundance of ammoniated phyllosilicates. However, these artifacts do not affect the measured 3.4-μm spectral parameters since each 3.4-μm absorption band is fitted by a polynomial curve. The 3.4 μm absorption band in the mean spectrum of the Sintana ccp (pink spectrum) is mainly due to ammoniated phyllosilicates but given the similar abundance to that of Ceres average, the secondary absorption at 3.3 μm is not as evident as in Chaminuka ccp. Furthermore, the 3.4 μm band shape is not as round as for Abellio and CCP25, likely due to the depletion of carbonates. The contribution of NH_4-phyllosilicates in the 3.4-μm band of Haulani (yellow spectrum) and Ikapati ccp (blue spectrum) is minimal; in fact, the 3.3-μm absorption is almost absent, and the round shape is more evident. The shape of the 3.4-μm spectral feature in the Ernutet ccp (red spectrum) is intermediate between the Chaminuka ccp and the Haulani/Ikapati ccps: the contribution of ammoniated phyllosilicates is evident from the obvious 3.3-μm absorption; organics and carbonates, furthermore, are probably responsible of the very strong band, and the round shape.

7. Conclusions

The central uplifts of complex craters are the result of material uplifted from the subsurface as a consequence of a significant impact event. By analyzing spectral parameters of 32 ccps, we investigated the mineralogical composition of Ceres subsurface to a pseudo-depth of about 22 km. Based on the models that describe the interior of the

dwarf planet (Park et al., 2016; Ermakov et al., 2017; Fu et al., 2017), our investigation involved inner layers of crust and approached to the density discontinuity between volatile-rich crust and silicate-rich mantle, supposed to lie at depth of about 41 km (Ermakov et al., 2017).

The subsurface of Ceres is mainly composed of Mg/Ca-carbonates, Mg-phyllosilicates, NH_4-phyllosilicates and a featureless dark component, also contributing to its surface composition. The different abundance of carbonates and NH_4-phyllosilicates in Cerean ccps, in addition to organics, affects the shape of the absorption band located at about 3.4 μm.

Three ccps, i.e., Haulani, Ikapati and Ernutet, are composed of a mixture of Na-carbonates and Mg/Ca-carbonates, in addition to phyllosilicates and dark material. Ccps composed of Na-carbonates were uplifted from a pseudo-depth of about 6–9 km.

Subsurface deposits richer in Mg-phyllosilicates and ammoniated phyllosilicates are located at poleward latitudes. Furthermore, ammoniated clays are more concentrated in ccps that were excavated from greater depth.

Acknowledgments

VIR is funded by the Italian Space Agency–ASI and was developed under the leadership of INAF-Istituto di Astrofisica e Planetologia Spaziali, Rome-Italy. The instrument was built by Selex-Galileo, Florence-Italy. The authors acknowledge the support of the Dawn Science, Instrument, and Operations Teams. This work was supported by ASI and NASA.

References

Ammannito, E., et al., 2016. Distribution of phyllosilicates on the surface of Ceres. Science 353, aaf4279. http://dx.doi.org/10.1126/science.aaf4279.

Baratoux, D., et al., 2007. Mineralogical structure of the subsurface of Syrtis Major from OMEGA observations of lobate ejecta blankets. J. Geophys. Res. 112, E08S05. http://dx.doi.org/10.1029/2007JE002890.

Bishop, J.L., et al., 2002. Detection of soluble and fixed NH4+ in clay minerals by DTA and IR reflectance spectroscopy: a potential tool for planetary surface exploration. Planet. Space Sci. 50, 11–19. http://dx.doi.org/10.1016/S0032-0633(01)00077-0.

Carrozzo, F.G., et al., 2016. Artifacts reduction in VIR/Dawn data. Rev. Sci. Instrum. 87 (12), 124501.

Carrozzo, F.G., et al., 2018. Nature, formation and distribution of carbonates on Ceres. Sci. Adv. 4 (3). http://dx.doi.org/10.1126/sciadv.1701645.

Castillo-Rogez, J.C., McCord, T.B., 2010. Ceres' evolution and present state constrained by shape data. Icarus 205, 443–459. http://dx.doi.org/10.1016/j.icarus.2009.04.008.

Castillo-Rogez, J.C., 2011. Ceres – Neither a porous nor salty ball. Icarus 215 (2), 599–602. http://dx.doi.org/10.1016/j.icarus.2011.08.007.

Clark, R.N., Roush, T.L., 1984. Reflectance spectroscopy: quantitative analysis techniques for remote sensing applications. J. Geophys. Res. 89 (Nr. B7), 6329–6340. http://dx.doi.org/10.1029/JB089iB07p06329.

Cloutis, E.A., et al., 2011. Spectral reflectance properties of carbonaceous chondrites: 1. CI chondrites. Icarus 212, 180–209. http://dx.doi.org/10.1016/j.icarus.2010.12.009.

Combe, J.-Ph., et al., 2016. Detection of H_2O-rich materials on Ceres by the dawn mission. In: Proceedings of the 47th Lunar and Planetary Science Conference.

Combe, J.-Ph., et al., 2018. Exposed H_2O-rich areas detected on Ceres with the dawn visible and infrared mapping spectrometer, Icarus, in press.

De Sanctis, M.C., et al., 2011. The VIR Spectrometer. Space Sci. Rev. 163, 329–369. http://dx.doi.org/10.1007/s11214-010-9668-5.

De Sanctis, M.C., et al., 2015. Ammoniated phyllosilicates with a likely outer Solar System origin on (1) Ceres. Nature 528, 241–244. http://dx.doi.org/10.1038/nature16172.

De Sanctis, M.C., et al., 2016. Bright carbonate deposits as evidence of aqueous alteration on (1) Ceres. Nature 536 (7614), 54–57. http://dx.doi.org/10.1038/nature18290.

De Sanctis, M.C., et al., 2017. Localized aliphatic organic material on the surface of Ceres. Science 355 (6326), 719–722. http://dx.doi.org/10.1126/science.aaj2305.

Dence, M.R., 1968. Shock zoning at Canadian craters: Petrography and structural implications. In *Shock Metamorphism of Natural Materials* (B.M. French and N.M. Short, eds.), pp. 169–184, Mono Book Corp. Baltimore.

Engel, S., Lunine, J.I., Norton, D.L., 1994. Silicate interactions with ammonia-water fluids on early Titan. J. Geophys. Res. 99, 3745–3752. http://dx.doi.org/10.1029/93JE03433.

Ermakov, A.I., et al., 2017. Constraints on Ceres' internal structure and evolution from its shape and gravity measured by the Dawn spacecraft. J. Geophys. Res. Planets 122, 2267–2293. http://dx.doi.org/10.1002/2017JE005302.

Fu, R.R., et al., 2017. The interior structure of Ceres as revealed by subsurface topography. Earh Planet. Sci. Lett. 476, 153–164. http://dx.doi.org/10.1016/j.epsl.2017.07.053.

Galiano, A., et al., 2018. Continuum definition for ~3.1. ~3.4 and ~4.0 μm absorption bands in Ceres spectra and evaluation of effects of smoothing procedure in the retrieved spectral parameters, Adv. Space Res., in press, https://doi.org/10.1016/j.asr.2017.10.039.

Gillis-Davis, J.J., 2016. Laser space weathering of possible (1) Ceres analogs. In: Proceedings of the 47th Lunar and Planetary Science Conference.

Grieve, R.A.F., et al., 1977. Cratering process: as interpreted from the occurrence of impact melts. In *Impact and Explosion Cratering: Planetary and Terrestrial Implications* (D.J. Roddy, R.O. Pepin, and R.B. Merrill, eds.), pp. 791–814, Pergamon, New York.

Grieve, R.A.F., et al., 1981. Constraints on the formation of ring impact structures, based on terrestrial data. In Multi-Ring Basins: Formation and Evolution. Proceedings of the Lunar and Planetary Science 12A (P.H. Schultz and R.B. Merrill, eds.), pp. 37–57, Pergamon, New York.

Grieve, R.A.F., 1991. Terrestrial impact: the record in the rocks. Meteoritics 26, 175–194.

Grieve, R.A.F., Pilkington, M., 1996. The signature of terrestrial impacts. AGSO J. Aust. Geol. Geophys. 16, 399–420.

Johnson, T.V., Fanale, F.P., 1973. Optical properties of carbonaceous chondrites and their relationship to asteroids. J. Geophys. Res. 78 (35), 8507–8518. http://dx.doi.org/10.1029/JB078i035p08507.

Hiesinger, H., et al., 2016. Cratering on Ceres: Implication for its crust and evolution. Science 353 (6303). http://dx.doi.org/10.1126/science.aaf4759.

Hughson, K.H.G., et al., 2017. The Ac-H-5 (Fejokoo) quadrangle of Ceres: geologic map and geomorphological evidence for ground ice mediated surface processes. Icarus, in press. http://dx.doi.org/10.1016/j.icarus.2017.09.035.

Ivanov, B.A., et al., 1982. Formation of the central uplift in meteoritic craters. Meteoritika 40, 67–81 in Russian.

Kieffer, S.W., Simonds, C.H., 1980. The role of volatiles and lithology in the impact cratering process. Rev. Geophys. Space Phys. 18, 143–181. http://dx.doi.org/10.1029/RG018i001p00143.

King, T.V.V., et al., 1992. Evidence for ammonium-bearing minerals on Ceres. Science 255, 1551–1553. http://dx.doi.org/10.1126/science.255.5051.1551.

Kneissl, T., et al., 2016. Geologic mapping of the Ac-H-3 Dantu quadrangle of Ceres from NASA's dawn mission. In: Proceedings of the 47th Lunar and Planetary Science Conference.

Krohn, K., et al., 2017. The unique geomorphology and structural geology of the Haulani crater of dwarf planet Ceres as revealed by geological mapping of equatorial quadrangle Ac-6 Haulani. Icarus in press. https://doi.org/10.1016/j.icarus.2017.09.014.

Lantz, C., et al., 2017. Ion irradiation of carbonaceous chondrites: a new view of space weathering on primitive asteroids. Icarus 285, 43–57. http://dx.doi.org/10.1016/j.icarus.2016.12.019.

Longobardo, A., et al., 2014. Photometric behavior of spectral parameters in Vesta dark and bright regions as inferred by the Dawn VIR spectrometer. Icarus 240, 20–35. http://dx.doi.org/10.1016/j.icarus.2014.02.014.

Longobardo, A., et al., 2018a. Mineralogy of the Urvara-Yalode region on Ceres. Icarus. http://dx.doi.org/10.1016/j.icarus.2017.12.011. in press.

Longobardo, A., et al., 2018b. Mineralogy of Occator quadrangle. Icarus in press. https://doi.org/10.1016/j.icarus.2017.09.022.

Maxwell, D.E., et al., 1977. Simple Z model of cratering, ejection, and the overturned flap. In *Impact and Explosion Cratering: Planetary and Terrestrial Implications* (D.J. Roddy, R.O. Pepin, and R.B. Merrill, eds.), pp. 1003–1008, Pergamon New York.

McCord, T.B., Sotin, C., 2005. Ceres: evolution and current state. J. Geophys. Res. 110, E05009. http://dx.doi.org/10.1029/2004JE002244.

Melosh, H.J., 1989. Impact Cratering: A Geologic Process. Oxford University, New York, pp. 245.

Mest, S.C., et al., 2018. Hamo-based global geologic map and chronostratigraphy of Ceres. In: Proceedings of the 49th Lunar and Planetary Science Conference.

Moroz, L.V., et al., 1998. Natural solid bitumens as possible analogs for cometary and asteroid organics: 1. Reflectance spectroscopy of pure bitumens. Icarus 134 (2), 253–268. http://dx.doi.org/10.1006/icar.1998.5955.

Nathues, A., et al., 2015. Sublimation in bright spots on (1) Ceres. Nature 528 (7581), 237–240. http://dx.doi.org/10.1038/nature15754.

Nathues, A., et al., 2017. Evolution of Occator Crater on (1) Ceres. Astronomical J. 153 (3), 12. http://dx.doi.org/10.3847/1538-3881/153/3/112.

Neveu, M., et al., 2017. Aqueous geochemistry in icy world interiors: Equilibrium fluid, rock, and gas compositions, and fate of antifreezes and radionuclides. Geochimica et Cosmochimica Acta 212, 324–371.

Nuevo, M., et al., 2014. Mid-infrared study of stones from the Sutter's Mill meteorite. Meteor. Planet. Sci. 49 (11), 2017–2026. http://dx.doi.org/10.1111/maps.12269.

O'Brien, D.P., et al., 2014. Constraining the cratering chronology of Vesta. Planet. Space Sci. 103, 131–142. http://dx.doi.org/10.1002/2016GL071143.

O'Keefe, J.D., Ahrens, T.J., 1982. Cometary and meteorite swarm impact on planetary surfaces. J. Geophys. Res. 87 (Nr. B8), 6668–6680. http://dx.doi.org/10.1029/JB087iB08p06668.

O'Keefe, J.D., Ahrens, T.J., 1993. Planetary cratering mechanics. J. Geophys. Res. 98, 17011–17028. http://dx.doi.org/10.1029/93JE01330.

Palomba, E., et al., 2018. Compositional differences among Bright Spots on the Ceres surface. Icarus in press. https://doi.org/10.1016/j.icarus.2017.09.020.

Pan, C., et al., 2015. Thermal and near-infrared analyses of central peaks of Martian impact craters: evidence for a heterogeneous Martian crust. J. Geophys. Res. Planets 120, 662–688. http://dx.doi.org/10.1002/2014JE004676.

Park, R.S., et al., 2016. A partially differentiated interior for (1) Ceres deduced from its gravity field and shape. Nature 537, 515–517. http://dx.doi.org/10.1038/nature18955.

Pasckert, J.H., et al., 2017. Geologic map of the Ac-2-Coniraya quadrangle of Ceres from NASA's dawn mission: implication for a heterogeneously composed crust, Icarus, in press, doi:10.1016/j.icarus.2017.06.015.

Pieters, C.M., et al., 1997. Mineralogy of the mafic anomaly in the South Pole Aitken basin: implications for excavation of the lunar mantle. Geophys. Res. Lett. 24 (15), 1903–1906. http://dx.doi.org/10.1029/97GL01718.
Pieters, C.M., Noble, S.K., 2016. Space weathering on airless bodies. J. Geophys. Res. Planets 121, 1865–1884. http://dx.doi.org/10.1002/2016JE005128.
Pinet, P.C., et al., 1993. Copernicus: a regional probe of the lunar interior. Science 206 (5109), 797–801. http://dx.doi.org/10.1126/science.260.5109.797.
Platz, T., et al., 2016. Surface water-ice deposits in the northern shadowed regions of Ceres. Nature Astron. 1 (0007), 1–6. http://dx.doi.org/10.1038/s41550-016-0007.
Raponi, A., et al., 2017. Mineralogical mapping of Coniraya quadrangle of the dwarf planet Ceres. Icarus. http://dx.doi.org/10.1016/j.icarus.2017.10.023.
Raponi, A., et al., 2018a. Mineralogy of Occator crater on Ceres and insight into its evolution from the properties of carbonates, phyllosilicates and chlorides. Icarus, in press, https://doi.org/10.1016/j.icarus.2018.02.001.
Raponi, A., et al., 2018b. Variations in the amount of water ice on Ceres's surface suggest a seasonal water cycle. Sci. Adv. 4 (Nr.3). http://dx.doi.org/10.1126/sciadv.aao3757.
Rivkin, A.S., et al., 2011. The surface composition of Ceres. Space Sci. Rev. 163, 95–116. http://dx.doi.org/10.1007/s11214-010-9677-4.
Ruesch, O., et al., 2016. Cryovolcanism on Ceres. Science 353 (6303). http://dx.doi.org/10.1126/science.aaf4286.
Russell, C.T., et al., 2015. Dawn arrives at Ceres; results of the survey orbit. Eur. Planet. Sci. Congr. Abstract 10 and page 14.
Russell, C.T., et al., 2016. Dawn arrives at Ceres: Exploration of a small, volatile-rich world. Science 353 (6303), 1008–1010. http://dx.doi.org/10.1126/science.aaf4219.
Schmedemann, N., et al., 2014. The cratering record, chronology and surface ages of (4) Vesta in comparison to smaller asteroids and the ages of HED meteorites. Planet. Space Sci. 103, 104–130. http://dx.doi.org/10.1016/j.pss.2014.04.00410.1002/2016GL071143.
Schmedemann, N., et al., 2016. Timing of optical maturation of recently exposed material on Ceres. Geophys. Res. Lett. 43, 11987–11993. http://dx.doi.org/10.1002/2016GL071143.
Schenk, P.M., et al., 2016. Central pit and dome formation as seen in Occator Crater, Ceres. In: Proceedings of the AAS/Division for Planetary Sciences Meeting Abstracts.
Schulzeck, F., et al., 2017. Geologic mapping of the Ac-H-11 Sintana quadrangle: assessing diverse crater morphologies. Icarus, in press. http://dx.doi.org/10.1016/j.icarus.2017.12.007.
Scully, J.E.C., et al., 2017. Ceres' Ezinu quadrangle: a heavily cratered region with evidence for localized subsurface water ice and the context of Occator crater. Icarus, in press. http://dx.doi.org/10.1016/j.icarus.2017.10.038.
Stephan, K. et al., 2018, Ceres' craters-relationships between surface composition and geology, Icarus, in press, doi:10.1016/j.icarus.2017.10.013.
Tornabene, L.L., et al., 2008. Surface and crater-exposed lithologic units of the Isidis Basin as mapped by coanalysis of THEMIS and TES derived data products. J. Geophys. Res. 113, E10001. http://dx.doi.org/10.1029/2007JE002988.
Travis, B.J., Feldman, W.C., 2016. Ceres model suggests large scale topography may reflect early time internal convection. In: Proceedings of the 47th Lunar and Planetary Science Conference.
Vinogradoff, V., et al., 2018. Insight into the nature and formation of the organic matter observed on Ceres. Astrophys. J in press.
Vu, T.H., et al., 2017. Preferential formation of sodium salts from frozen sodium-ammonium-chloride-carbonate brines – Implication for Ceres bright spots. Planet. Space Sci. 141, 73–77. http://dx.doi.org/10.1016/j.pss.2017.04.014.
Williams, D.A., 2018. Unified Dawn Lamo-based global geologic map of Ceres. In: Proceedings of the 49th Lunar and Planetary Science Conference.
Zambon, F., et al., 2017. Spectral analysis of Ahuna Mons from Dawn mission's visible-infrared spectrometer. Geophys. Res. Lett. 44 (1), 97–104. http://dx.doi.org/10.1002/2016GL071303.
Zolotov, M.Y., 2017. Aqueous origins of bright salt deposits on Ceres. Icarus 296, 289–304. http://dx.doi.org/10.1016/j.icarus.2017.06.018.

Sitography

https://planetarynames.wr.usgs.gov/nomenclature/SearchResults.
https://www.jpl.nasa.gov/spaceimages/details.php?id=PIA19974.